International Reviews in Physical Chemistry
Vol. 31, No. 2, April–June 2012, 265–318

Time-resolved photoelectron spectroscopy of non-adiabatic electronic dynamics in gas and liquid phases

Toshinori Suzuki[abc]*

[a]*Department of Chemistry, Graduate School of Science, Kyoto University, Kyoto 606-8502, Japan;* [b]*CREST, Japan Science and Technology Agency, Tokyo 102-0075, Japan;* [c]*RIKEN Advanced Science Institute, RIKEN, Wako 351-0851, Japan*

(*Final version received 4 May 2012*)

Time-resolved photoelectron spectroscopy of non-adiabatic processes in isolated molecules in molecular beams and aqueous solutions at ambient temperatures is discussed. In the former, time–energy mapping of photoelectron kinetic energy and angular distributions is performed with 22 fs time-resolution by photoelectron imaging using a multicolour filamentation light source. The S_2–S_1 internal conversion dynamics in pyrazine, benzene and toluene mediated by conical intersections and deactivation of furan from the Rydberg and valence states are discussed. In the latter, a liquid beam photoelectron spectrometer (hemispherical or time-of-flight) is coupled with a sub-MHz non-collinear optical parametric amplifier. Additionally, charge-transfer-to-solvent reactions from I^- to polar protic solvents are observed, and the vertical electron binding energies of solvated electrons in bulk solutions are determined.

Keywords: ultrafast; photoelectron spectroscopy; imaging; non-adiabatic; internal conversion; pyrazine; benzene; toluene; furan; charge transfer; solvated electron

Contents

---

*Email: suzuki@kuchem.kyoto-u.ac.jp

ISSN 0144–235X print/ISSN 1366–591X online

http://dx.doi.org/10.1080/0144235X.2012.699346
http://www.tandfonline.com

1. Introduction

For many years, one of the greatest desires of all chemists has been real-time observation of the entire chemical reactions, from reactants to products. Its realisation, however, is extremely difficult for bimolecular reactions, even at the present time, because the timing of molecular encounters can hardly be controlled with higher precision than the reaction time. On the other hand, photo-induced reactions can be triggered with ultrashort laser pulses, and evolution of the non-stationary states is revealed with the pump–probe methods. The time-resolution in ultrafast spectroscopy has been improving continuously since the pioneering flash photolysis experiments of the 1950s [1–3]. Femtochemistry presented by Zewail [4] and coworkers was the milestone in this endeavour. The highest time-resolution has now reached ca. 100 attosecond, albeit in limited wavelength region [5–7].

The best probe method of each reaction depends on the information most important for elucidation of its mechanism. X-ray diffraction/scattering has been used for the structural analysis of large (bio)molecules at the third-generation synchrotron facilities [8–10], and high-intensity X-ray free electron lasers are opening a new avenue for the structural analysis of non-crystalline samples and nanocrystals [11,12]. Femtosecond time-resolved X-ray diffraction/scattering/absorption spectroscopies will be realised in the near future in combination of X-ray free electron lasers with femtosecond solid-state lasers. Ultrafast electron diffraction has been demonstrated most notably for solids [13–18]. A question may arise as to whether clear diffraction or scattering patterns are observable after a vibrational wave packet of a photoexcited molecule spreads over a large phase–space volume; the answer is not known at present and will depend on molecule and excess vibrational energy. Vibrational spectroscopy (infrared and Raman) is a well-established non-invasive probe of a functional group in the solution, and it has played a central role in studying biophysical/biochemical processes [19–24]. Complex vibrational spectra of large biomolecules are resolved using the resonance Raman effect, isotope labelling and substitution of functional groups. Transient absorption, emission and photoelectron spectroscopies [25–27] are necessary for elucidating the electron dynamics that induce the molecular structural changes. In fact, the electronic deactivation pathways and their quantum yields are crucial for understanding photochemical reaction mechanisms, while they are generally not understood for large polyatomic molecules [28,29].

In this article, I describe our most recent studies on non-adiabatic electronic dynamics of polyatomic molecules using time-resolved photoelectron spectroscopy (TRPES) [30–40].

An exhaustive survey of the literature is not attempted here, as other researchers in the field have beautifully accomplished that task [39,41]. I will rather focus on summarising our studies in the past three years. Technical aspects, such as ultrafast lasers and electron spectrometers, are also described briefly.

2. TRPES: time–energy mapping of observables

Photoelectron spectroscopy was developed by Siegbahn [42,43], Turner [44,45], Vilesov [46] and their coworkers from the late 1950s to early 1960s and has played an important role in the development of a molecular orbital theory [37]. Figure 1 shows the diagram of a He(I) ultraviolet (UV) photoelectron spectrometer beautifully designed by Al-Joboury and Turner [47]. UV photoelectron spectroscopy analyses photoemission from valence orbitals that play essential roles in determining molecular structures and dynamics. X-ray photoelectron spectroscopy observes inner-shell electrons that have almost no contribution to chemical bonding and reactions yet whose energies exhibit the 'chemical shifts' that are useful for probing chemical bonding state of an atom [25–27,43]. X-ray photoelectron spectroscopy is also termed as electron spectroscopy for chemical analysis (ESCA).

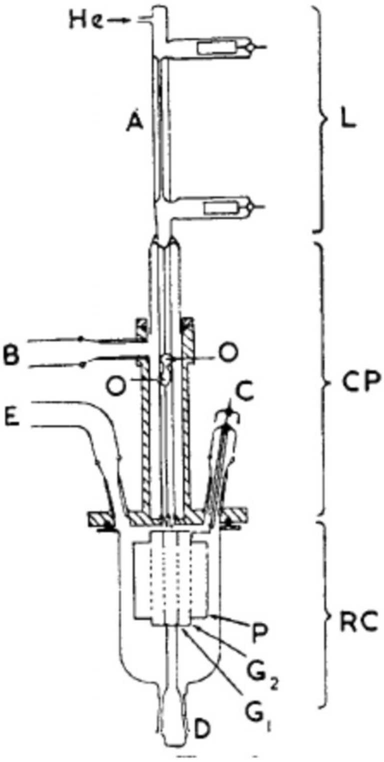

Figure 1. He(I) photoelectron spectrometer by Al-Joboury and Turner, diagram reported in 1963. L, light source of He(I) radiation ($h\nu = 21$ eV); CP, collimator and differential pumping section and RC, retarding-field grid chamber. Reprinted with permission from Ref. [47] (Copyright 1963 Royal Society of Chemistry).

TRPES was initiated in 1980s and has enabled unprecedented access to electronic dynamics in isolated molecules, clusters and surfaces [30–41,48–51]. Although bulk liquids have long been excluded as a target of TRPES owing to experimental difficulties, TRPES of liquids currently receives vital challenges by experimentalists as the 'final' frontier. TRPES of liquids is described later in Section 6.

The experimental observables in photoelectron spectroscopy are the velocity (speed and angle) and spin of a photoelectron; the spin state, however, is analysed almost exclusively for studying magnetic properties of solids using a special detector (the Mott detector [52,53] or spin-polarised low-energy-electron-diffraction detector [54–57]). Thus, the primary observable is speed (or kinetic energy) of a photoelectron, which carries fundamental spectroscopic information such as the ionisation energy, and electronic and vibrational energies of the cation. The photoelectron kinetic energy distribution observed for ionisation to each cationic electronic state exhibits Franck–Condon distribution (or envelope), which manifests molecular structural deformation upon the removal of an electron, enabling assignment of the ionised orbital [25]. Various instruments are available for measurements of photoelectron kinetic energy distributions. A hemispherical analyser is the unique instrument combined with (pseudo-)continuous light sources, such as synchrotron radiation, microwave discharge lamps and high-repetition rate lasers ($>1\,\mathrm{MHz}$), and it provides unrivaled high-energy resolution. A time-of-flight (TOF) analyser is used with pulsed light sources; a magnetic bottle TOF analyser provides a large detection solid angle of 2π steradian [58]. A photoelectron imaging analyser achieves the ultimate solid angle of 4π steradian and, more importantly, the ability to measure the photoelectron kinetic energy distribution and photoelectron angular distribution (PAD) simultaneously [37,38]. Both the TOF and imaging spectrometers can observe the entire photoelectron kinetic energy distribution on the shot-to-shot basis, which enables rapid data acquisition.

The photoelectron ejection angle is an important observable in photoelectron spectroscopy. Since the initial ensemble of molecules has an isotropic molecular axis distribution in the absence of external field, it is an isotropic target for photoionisation, similarly with the 1s orbital of a hydrogen atom. Therefore, the anisotropy of the total physical system (molecule + radiation) prior to photoionisation is caused by polarised photons. This anisotropy is transferred to PAD after photoionisation. When ionisation is induced by n-photon process, PAD is expanded with spherical harmonics up to the $2n$-th order (the odd orders are excluded, except for photoionisation of chiral molecules with circularly polarised light): more accurately, the rank and component of the anisotropy of PAD are related to those of state multipoles of the laser field [59]. (This is only true for perturbation regime of light-matter interaction: in a strong field, an electronic transition undergoes Rabi cycling and the resonant n-photon excitation can create polarisation of the system higher than the $2n$-th order, because $2n(2m+1)$ photon processes can occur by Rabi cycles ($m = 0, 1, 2, \ldots$) [34,60,61]. In this article, however, I discuss only the experiments in the perturbation regime, where complication induced by strong fields is safely neglected.) When polarisation of the pump and probe pulses are linear and parallel to each other, the overall system has cylindrical symmetry around the polarisation. Then, PAD can be expanded with Legendre polynomials, instead of spherical harmonics, because there is no azimuthal angle dependence [37,38]. Thus, the photoelectron kinetic energy and angular distribution in $(1+1')$ photoionisation is expressed as follows (the prime means different colour):

$$I(E,\theta,t) = \frac{\sigma(E,t)}{4\pi}\{1 + \beta_2(E,t)P_2(\cos\theta) + \beta_4(E,t)P_4(\cos\theta)\} \tag{1}$$

where E, θ and t are the photoelectron kinetic energy, the electron ejection angle from the laser polarisation direction, and the pump-probe time delay. $P_n(x)$ are the n-th order Legendre polynomials. $\sigma(E,t)$ represents a photoelectron kinetic energy distribution or photoelectron spectrum. $\beta_2(E,t)$ and $\beta_4(E,t)$ are called anisotropy parameters. The three scalar quantities $\sigma(E,t)$, $\beta_2(E,t)$ and $\beta_4(E,t)$ in Equation (1) are the observables in $(1+1')$ TRPES (or TRPEI: time-resolved photoelectron imaging) of gaseous samples. Extraction of dynamical information from $\beta_2(E,t)$ and $\beta_4(E,t)$ is the heart of TRPEI.

Let us assume that we excite a molecule from S_0 to S_2 with the pump pulse and ionise it to cationic states with the probe pulse. In the schematic diagram shown in Figure 2, the probe photon energy is sufficiently high to induce ionisation to the three lowest electronic states, D_0, D_1 and D_2, of the cation: the corresponding photoelectron kinetic energy distribution is shown on the left side. The shapes of the D_0, D_1 and D_2 photoelectron bands are determined by the Franck–Condon factors between S_2 and D_0, D_1 and D_2, and the intensity ratios of the D_0, D_1 and D_2 bands are determined by the electric transition dipole moments from S_2 to these states. When the nuclear wave packet moves from the Franck–Condon region to elsewhere on the S_2 potential energy surface, not only the Franck–Condon factors but also the dipole moments can change, because the electron

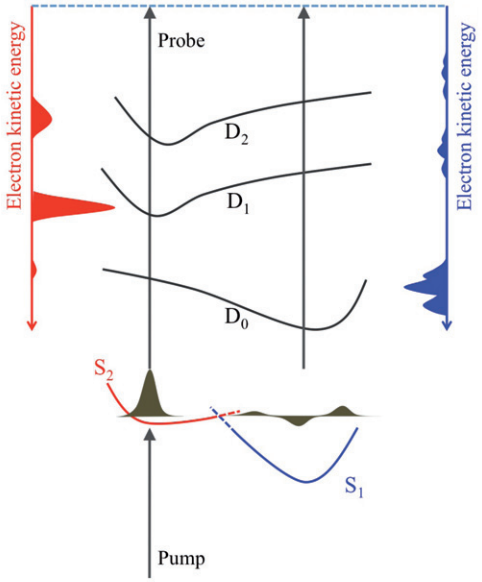

Figure 2. (Colour online) Schematic diagram of TRPES and kinetic energy distributions. The photoelectron kinetic energy distribution observed for photoionisation from the Franck–Condon region of S_2–S_0 transition is shown on the left, while the distribution observed for photoionisation from S_1 manifold with a time-delayed probe pulse is shown on the right.

wavefunction depends on a nuclear geometry. This dependence is sufficiently small to be neglected (Condon approximation) if nuclear displacement is very small. The approximation, however, becomes invalid when the nuclear displacement is extensive, e.g. from planar to non-planar or from linear to bent. Drastic changes of the transition dipole moments can occur, when the electronic state changes from one diabatic state to the other. In Figure 2, the S_1 state is populated by internal conversion from S_2, and photoionisation with a time-delayed probe pulse from S_1 creates a photoelectron kinetic energy distribution shown on the right side.

Photoionisation to multiple cationic states generally requires a vacuum UV probe pulse. When a UV probe pulse is used, ionisation may be induced only to D_0. In such cases, electronic deactivation is detected from time-evolution of the Franck–Condon factor in $\sigma(E, t)$. For example, if the pump pulse prepares a vibrational wave packet at the potential minimum of S_2, the Franck–Condon factor for ionisation is time-independent in the absence of electronic deactivation. When electronic deactivation occurs to S_1, the S_2–S_1 electronic energy difference is transformed into the vibrational energy in S_1 and the Franck–Condon factor for ionisation changes. The dynamics becomes more complex, however, when the initial wave packet is prepared in highly vibrationally excited states in S_2, because intramolecular vibrational redistribution within S_2 can also cause time-evolution of the Franck–Condon factor.

Let us now turn to PAD. By neglecting antisymmetrisation of the wave function, the electronic wave function of the final state, $|f\rangle$, of photoionisation is expressed as $|f\rangle = |\text{ion}\rangle|k(E)\rangle$ using the electronic wave function of a cation, $|\text{ion}\rangle$, and the photoelectron wave function, $|k(E)\rangle$. If the independent electron approximation is applied, the electric transition dipole moment is simplified as $\langle k(E)|er|\phi_a\rangle$ where ϕ_a is the ionised one-electron orbital (from which an electron is removed upon ionisation), and e and r are the elementary charge and an electron coordinate. Since $|k(E)\rangle$ is expressed by a linear combination of the partial waves, such as atomic-like $s, p, d, \dots$ waves, the transition dipole moment is finally expressed by a linear combination of multiple terms. These terms interfere with each other and determine the PAD. The phase factors of the partial waves vary with the electron kinetic energy E, as a property of eigen wavefunctions in a Coulomb potential. Consequently, the interference of the multiple terms change PAD as a function of E. Each electron orbital $|\phi_a\rangle$ exhibits characteristic energy-dependence of photoelectron angular anisotropy, which provides a fingerprint of $|\phi_a\rangle$ [62–67]. (If shape resonance, formation of a metastable state against photoionisation, occurs in the final state $|f\rangle$, PAD exhibits anomalous behaviour. Nevertheless, since the occurrence of shape resonance strongly depends on the ionised orbital, the energy dependence of PAD still serves as a fingerprint of an ionised orbital.) Let us consider that electronic dephasing changes the singly occupied molecular orbital from an atomic-like s (ϕ_a) orbital to d (ϕ_b). Then, as far as the anisotropy of the molecular potential is low, ionisation from these orbitals create p wave and the mixture of p and f partial waves, respectively, and $\beta_2(E, t)$ diminishes upon the electronic dephasing.

In pump–probe experiments using femtosecond lasers, the pump pulse creates not only vibrational wave packet but also rotational wave packet: the pump pulse coherently excites P, Q and R rotational branches associated with an electronic transition and creates the molecular axis alignment. The axis alignment diminishes in less than several ps (rotational dephasing) and revives fully at much later time (~100 ps in benzene derivatives).

These rotational dynamics of photoexcited molecules influence the photoelectron angular anisotropy [68–70], and observation of the revival features of angular anisotropy serves as rotational coherence spectroscopy [71–74]. For example, $S_1 \rightarrow T_1$ intersystem crossing of pyrazine occurs in 110 ps, and TRPEI revealed rotational dynamics from S_1 to T_1 in time-dependent photoelectron anisotropy [68–70]. In this review, however, I will focus on ultrafast internal conversion that occurs in less than 100 fs, and the rotational effects can be neglected.

Theoretical simulation of TRPES of polyatomic molecules requires technical expertise in three factors, (a) computation of multiple electronic states, (b) multi-dimensional vibrational dynamics and (c) description of ionisation continua. Construction of multiple potential energy surfaces for polyatomic molecules is highly computationally demanding, so that dynamical calculations on the fly are often performed. The method encompasses quantum or classical mechanical calculations of nuclear motions by solving the electronic Schrödinger equation simultaneously at each nuclear geometry while avoiding the construction of potential energy surfaces. As for the vibrational dimensions of a molecule, most of them, if not all, should be taken into account, because some vibrational modes may be unimportant in the excited-state dynamics but still Franck–Condon active in the photoionisation process. The ionisation continua may be treated accurately by *R*-matrix [75] or Schwinger variational calculations [76], but it is difficult to apply these methods to large polyatomic molecules. Consequently, Stieltjes imaging or other approximation of the ionisation continua is employed [77–80]; these methods, however, do not allow calculations of PAD. Further development of computational methodologies is desirable to simulate time-dependent PAD for polyatomic molecules.

3. Ultrafast internal conversion via conical intersection

Based on the Born–Oppenheimer approximation [81], photophysical and photochemical processes can be viewed as classical trajectories or quantum mechanical wave packet motions of nuclear geometry on the potential energy surfaces made by electronic motions. When two potential energy surfaces become energetically close to each other, the Born–Oppenheimer approximation breaks down, which results in non-adiabatic transitions between the potential energy surfaces. The non-adiabatic transitions induce a variety of molecular processes, and their elucidation is the key for understanding complex dynamics, particularly of polyatomic molecules.

Conical intersection is the most important topographical features of the multi-dimensional surfaces that induce non-adiabatic dynamics in polyatomic molecules [83–87]. In a diatomic molecule, the von Neumann–Wigner [88] non-crossing rule prohibits degeneracy of the electronic states with the same symmetry, so that their potential energy curves create avoided crossing. In a polyatomic molecule with N internal degrees of freedom, potential energy surfaces can be degenerated to make a seam of crossings in $N-2$ dimensional space, which is termed as conical intersection. The characteristic conical shape of the surface funnels the nuclear trajectories on an upper surface down to a lower one, facilitating efficient internal conversion. Furthermore, the Born–Oppenheimer approximation breaks down not only at the seam of crossings but also in a wider region in its vicinity. Photodissociation of ammonia [89–92] and *cis–trans* isomerisation of ethylene [93,94] are the well-known examples for photochemical reactions mediated by

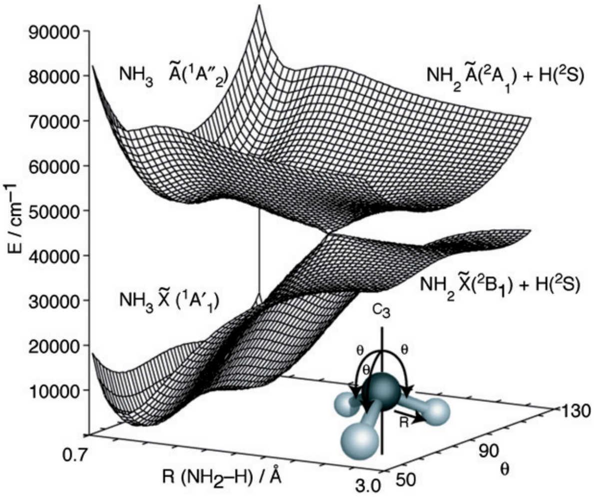

Figure 3. Potential energy surfaces for the A and X states of ammonia for the NH$_2$–H stretch and out-of-plane bending angle θ. Reprinted with permission from Ref. [82] (Copyright 2006 American Institute of Physics).

conical intersection (Figure 3). The ground electronic state of ammonia belongs to the C_{3v} point group (or the permutation-inversion group isomorphous to D_{3h}), while the first excited singlet state has a trigonal planar D_{3h} minimum. When the N–H bond is elongated in the planar geometry, the system becomes C_{2v} symmetry in which the excited and the ground-state potential energy surfaces are symmetry-allowed to intersect. In non-planar geometry, however, the two potential energy surfaces avoid each other, because the two electronic states fall into the same irreducible representation in the distorted geometry. (Notice, however, that not all conical intersections are attributed to the symmetries of the electronic states, as the electronic states of the same symmetry can intersect each other in polyatomic molecules.) The topography of the conical intersection, such as the symmetry and tilt angle of the apex, influences the non-adiabatic dynamics; the most important role in the dynamics, however, is played by the minimum energy conical intersection point, as it determines accessibility of the system to the seam of crossings.

In the late 1960s to early 1970s, researchers have realised that conical intersections play important roles in photophysical and photochemical processes of polyatomic molecules [95–97]. It was difficult, however, to identify conical intersections in high-dimensional configuration space. Developments of high-performance computers and advanced computational algorithms in quantum chemistry have made possible efficient computations of the potential energy surfaces and unveiled that conical intersections are ubiquitous in polyatomic molecules. As an example, Figure 4 shows a schematic diagram of the photochemical reaction pathways of benzene proposed by Palmer *et al.* [98].

For exploring ultrafast wave packet dynamics via conical intersection of multiple potential energy surfaces, the advantage of TRPES is that photoionisation is allowed from any electronic state and molecular geometry, if the photon energy is sufficiently high. Exploration of non-adiabatic dynamics in polyatomic molecules using TRPES is the subject of this review article.

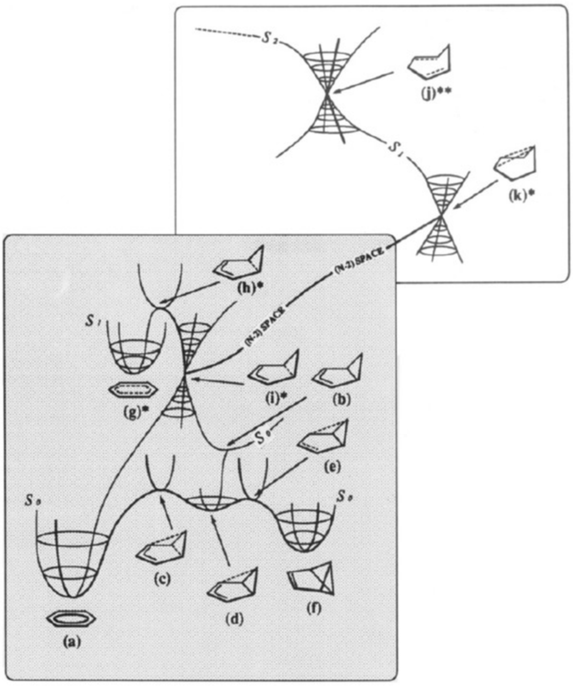

Figure 4. Photochemical reactions of benzene from S_2 and S_1 states mediated by conical intersections. Reprinted with permission from Ref. [98] (Copyright 1993 American Chemical Society).

4. Experimental techniques

4.1. *Photoelectron imaging*

TRPEI enables the most efficient and reliable measurements of PAD [38]. The method uses a static electric field to project the three-dimensional distribution of photoelectrons onto a two-dimensional position-sensitive detector. The acceleration field is designed, as demonstrated by Eppink and Parker [100], to make the projection image depend only on the velocities of electrons; thus, this method is called velocity map imaging. Although the simplest electrodes for the velocity map imaging consist of three plates, a larger number of electrodes improve the performance, as demonstrated by Lin *et al.* [101] The design of our electrodes is shown in Figure 5 [99]. A large square-shaped hole in the electrode 4 allows propagation of laser beams or He(I) radiation. The ionisation point is indicated with a cross (×). We designed the electrodes 1–3 to reduce background photoemission by stray light. The electrode 3 is a repeller plate, but it has a large hole in the centre to reduce background photoemission. In order to flatten the equipotential around the hole of the electrode 3, the electrode 2 is held at the same voltage with the electrode 3. The electrode 1 is used to prevent penetration of the ground potential into the acceleration electric field, while a high-transmission (90%) mesh minimises its cross section, and consequently, background photoemission from the electrode 1. The voltage of the electrode 1 is slightly higher than those of the electrodes 2 and 3, so that the photoelectrons emitted from the

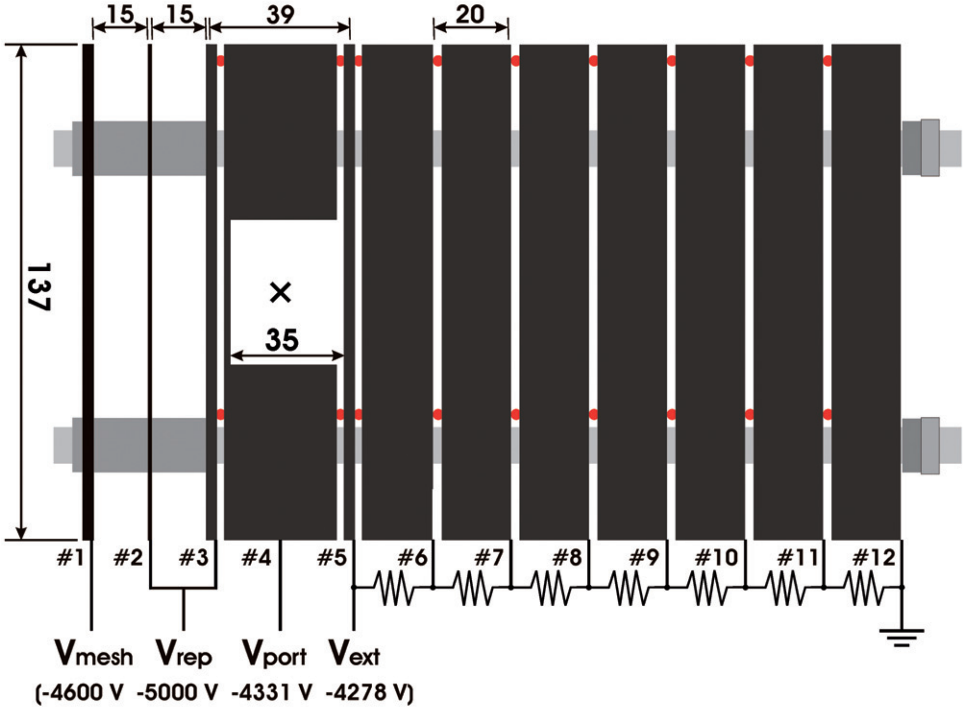

Figure 5. (Colour online) Cross-sectional view (left half) and front view (right half) of our electrostatic lens system (all units in millimetres). A molecular beam is introduced from the left and the ionisation point is indicated by the cross (×). Reprinted with permission from Ref. [99] (Copyright 2011 American Chemical Society).

electrode 1 by stray light are not transmitted towards the detector. The electrode 1 has a 6 mm diameter hole in the centre to allow the molecular beam to pass through in the direction parallel to the axis of the electrode stack. We computed electron trajectories and found that, although velocity resolution improves for even larger number of electrodes, it is practically saturated. The design shown in Figure 5 provides $\Delta\upsilon/\upsilon < 0.04\%$ for a focused laser beam.

Since the charged-particle optics is thus optimised, the remaining factors that limit the resolution are a camera and image-processing algorithm. Even if velocity map imaging electrodes focus electron trajectories with the same velocity into a 5 μm diameter channel of a microchannel plate, a light spot on the phosphor screen appears in a much larger size and causes blurring of a photoelectron image. Therefore, it is necessary to perform centre of gravity calculations on these light spots, sometimes down to the sub-pixel size of a digital camera, to recover the resolution achieved by velocity map imaging electrodes. Notice also that amplification of an electron pulse in a microchannel plate is stochastic, and the brightness of light spots on the phosphor screen fluctuates for every event. The gain of a microchannel also diminishes with the output current, so that a microchannel

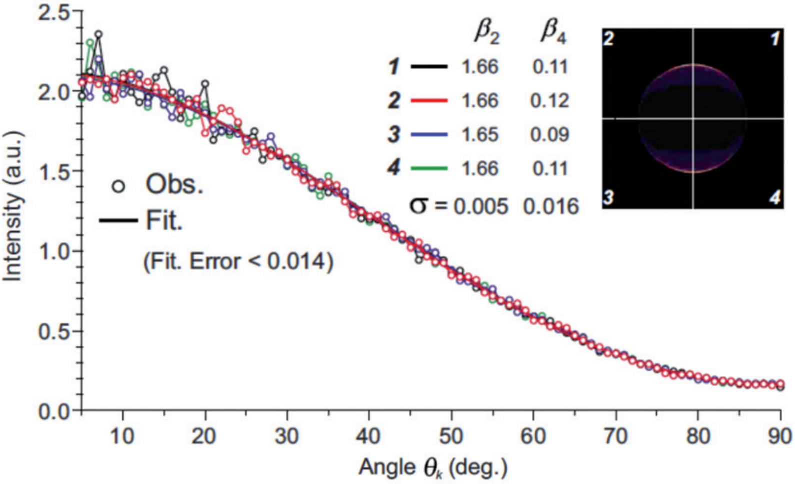

Figure 6. (Colour online) Representative examples of individual laboratory-frame PADs extracted from the four quadrants of an image shown in the inset. The observed distributions at each quadrant from one to four and the corresponding least squares fits of Equation (1) are shown with open circles and solid lines, respectively. The determined anisotropy parameter sets β_2, β_4 and their standard deviation obtained in each quadrant are shown. Reprinted with permission from Ref. [102] (Copyright 2009 American Institute of Physics).

plate eventually exhibits a burn pattern that degrades image quality. These problems can be solved by a two-dimensional electron counting algorithm [99,102,103]. Notice that both the centre of gravity calculations and the electron counting fail if light spots overlap one another; therefore, the frame rate of the camera must be comparable with or higher than the repetition rate (1 kHz) of a femtosecond laser. We constructed a 1 kHz camera using a complementary metal oxide semiconductor (CMOS) image sensor and a field programmable gate array circuit for real-time image processing. A CMOS sensor allows much faster readout than a charge-coupled-device (CCD) sensor, while the sensitivity of CMOS is considerably lower than CCD, at the present time. Thus, we used an image intensifier and booster to improve the sensitivity of our camera system; the detail is described in the original paper [102].

The performance of this imaging system is demonstrated in Figure 6, which shows the PADs in the four quadrants of a single image of $(1+1')$ resonance enhanced two-photon ionisation of nitric oxide [102,104]. The open circles are experimental values and the solid lines are the least squares fits of Equation (1). The anisotropy parameters β_2 and β_4 were determined with the standard deviations of 0.005 and 0.016, respectively. This is one of the most accurate determinations of anisotropy parameters in TRPES.

The observed photoelectron image corresponds to a two-dimensional projection of a three-dimensional photoelectron velocity distribution; therefore, the key step in the analysis of PAD is to calculate a slice through a three-dimensional velocity distribution from the observed image. An inverse Abel transform is a mathematical inversion method, and pBasex method is the least squares fitting of the data with a basis set [105]. These two methods generally provide comparable results; pBasex is, however, more reliable than the

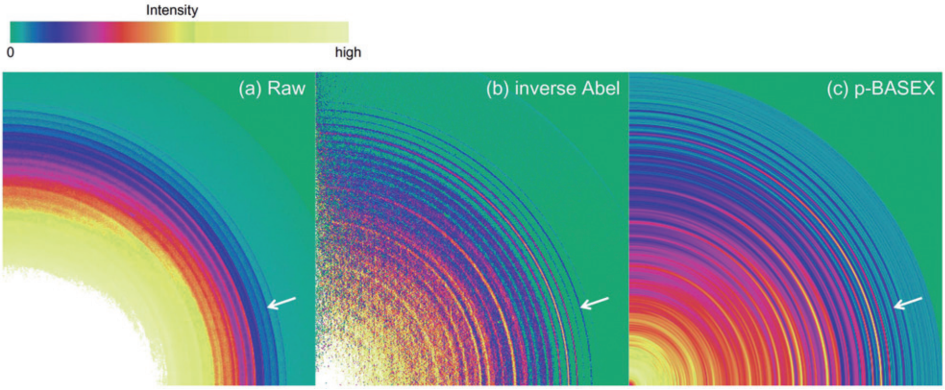

Figure 7. (a) False-colour raw image of $(1+1')$ resonance enhanced multiphoton ioinsation via $S_1 6^1 1^2$ of jet-cooled benzene, (b) a slice image calculated by an inverse Abel transform of (a) and (c) the same slice image calculated by pBasex method. The laser polarisation is in the vertical direction in the plane of images. The ring indicated by an arrow in (a) has more intensity in the direction perpendicular to the laser polarisation, which is not well reproduced in (b) due to numerical noises in inversion. (c) is consistent with (a). Reprinted with permission from Ref. [106] (Copyright 2011 American Chemical Society).

inverse Abel transform for low S/N images. For example, Figure 7 shows (a) a photoelectron image observed by $(1+1')$ photoionisation of benzene via the S_1 $6^1 1^2$ vibrational state using a nanosecond UV laser, (b) its inverse Abel transform and (c) a slice image obtained by pBasex [106]. The raw image (Figure 7a) shows that the outer ring indicated by an arrow exhibits a higher intensity at an ejection angle of 90° rather than 0° with respect to the laser polarisation, while Abel transformed image (Figure 7b) shows the opposite angular dependence. The original anisotropy is maintained in the image reconstructed by pBasex (Figure 7c). The difference of the two results is attributed to higher sensitivity of the inverse Abel transform to numerical noises.

4.2. *Deep UV sub-20 fs light source*

The femtosecond lasers that produce a pulse duration of ~100 fs are well-established as standard light sources for ultrafast spectroscopy [37,39]. A typical system uses a 1 kHz Ti:sapphire regenerative amplifier to pump two computer-controlled collinear parametric amplifiers that generate tunable UV pulses. We have used one such system for our TRPES over a decade and found it highly useful. On the other hand, internal conversion via conical intersection is extremely fast in aromatic molecules, and the real-time observation of these processes and associated vibrational wave packet dynamics necessitates time-resolution of the order of 20 fs. We have developed a sub-20 fs UV laser in our laboratory [107].

UV pulses (275–335 nm) with the duration of ~10 fs can be generated by achromatic frequency doubling of visible pulses [108]; it is difficult, however, to produce a wavelength shorter than 250 nm with such a short pulse duration. The other method to generate ~10 fs UV pulses is non-degenerate four-wave mixing in a hollow fibre filled with rare gas

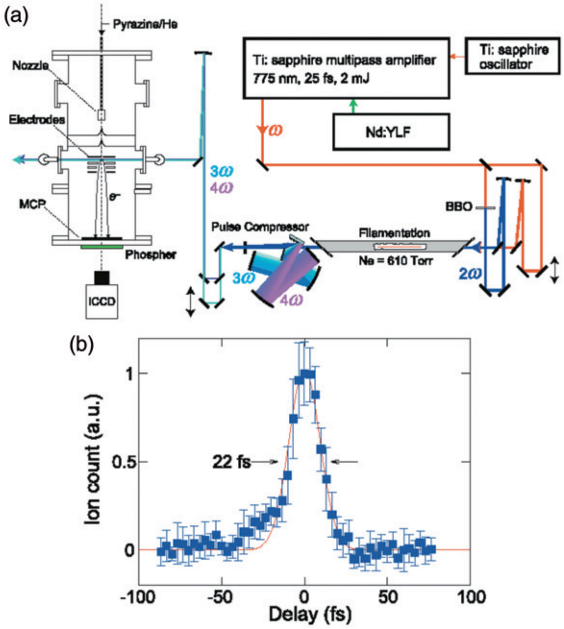

Figure 8. (Colour online) (a) Schematic diagram of filamentation four wave mixing to generate sub-20 fs deep UV pulses and our photoelectron imaging setup and (b) a typical cross-correlation trace between the pump and probe pulses obtained with a $(1+1')$ non-resonant photoionisation signal of ethanol in supersonic molecular beam. The red line shows Gaussian distribution with a full width at half maximum of 22 fs. Adapted with permission from Ref. [114] (Copyright 2010 American Institute of Physics).

[109,110]; this approach requires good pointing stability of the laser and careful alignment of the laser pulse into the narrow fibre channel.

We developed a simpler approach than the latter for non-degenerate four-wave mixing [107]. Filamentation propagation is a phenomenon by which an intense laser pulse propagates through a medium by maintaining a small beam diameter for a considerably greater length than a usual confocal parameter [111]. This is caused by self-focusing of the laser pulse due to an optical Kerr effect and simultaneous diffraction by the plasma created by ionisation of the medium. Figure 8(a) shows a schematic diagram of the light source and our imaging photoelectron spectrometer. The system starts with a cryogenically cooled Ti:sapphire linear amplifier that delivers 25 fs, 2.0 mJ and 775 nm pulses at 1 kHz. The fundamental beam (ω) is separated into two by the ratio 7:3, and the high-energy pulse is converted to the second harmonic(2ω), 0.5 mJ and ~30 fs, in a β-barium borate crystal. The second harmonic and the low-energy fundamental pulse (0.5 mJ) are gently focused into a rare gas cell filled with Ne (0.1 MPa). When these two pulses overlap temporally and spatially in the cell, a bright orange-coloured filament ~15 cm in length appears. Notice that the peak powers of these two laser pulses are lower than the critical power for self-focusing in Ne (160 and 40 GW at 775 and 388 nm) [112]; therefore, filamentation propagation is caused by the concerted interactions of multiple laser pulses with the gas medium. Filamentation induces ‘intensity cramping’ and ‘mode filtering’ to provide a stable energy and an excellent spatial mode of the output laser pulse [111]. Similar to four-wave mixing in a hollow fibre [110], filamentation four-wave mixing produces different harmonics in a single cell by cascaded non-linear processes: the mixing of ω and 2ω creates the 3ω(~260 nm), 4ω(~200 nm) and 5ω(~160 nm) pulses, simultaneously. This feature is extremely useful for TRPES, which requires two UV pulses for experiments. The maximum pulse energies of 3ω and 4ω are, respectively, 16 and 4 μJ. The pulse energy gradually diminishes for higher harmonics, as anticipated, but the intensity ratio of $4\omega/3\omega$ is higher in the filamentation than in the hollow fibre process. The gas–pressure dependence of four-wave mixing efficiency in filamentation is also different from the case of a follow fibre. The non-linear processes that create 3ω is $2\omega + 2\omega - \omega \rightarrow 3\omega$, while the gas–pressure dependence and theoretical calculations using a three-dimensional model of non-linear optical processes indicates that 4ω is created by two processes of $3\omega + 2\omega - \omega \rightarrow 4\omega$ and $2\omega + \omega + \omega \rightarrow 4\omega$ that interfere each other [113]. The 3ω and 4ω pulses are separated and compressed using a grating-based compressor (2400 lines/mm, 250 nm braze). The compressed outputs are *ca* 2.5 and 0.5 μJ for 3ω and 4ω, respectively. The two beams propagate through air and are focused into a photoelectron spectrometer with concave mirrors. The pulse durations of 3ω and 4ω are 14 and 17 fs, respectively.

4.3. *Deep UV 100 kHz light source*

Photoelectron imaging inevitably disperses electron signals over wide area of radial and angular coordinates; therefore, an image must be integrated over many laser shots to achieve good statistics. Early TRPEI experiments in our laboratory were performed with a 10 Hz YAG-based regenerative amplifier, and measurement of a single image took nearly an hour [70,115,116]. With such a long integration time required, study of detailed wave packet dynamics was not practical. A 1 kHz laser system has reduced the acquisition time of a single image to several minutes and made possible the detailed study of wave packet dynamics [38,68,69,117–122]. The repetition rate of a laser is particularly crucial for photoelectron spectroscopy, because the pulse energy must be sufficiently low to avoid creation of a space charge that distorts the photoelectron kinetic energy distribution. In application of TRPES to high-density liquid target, discussed later in this article, a space charge is more easily created than a gas target; therefore, UV pulse energy is reduced on the order of ~100 nJ. Thus, we constructed a 100 kHz laser system that generates deep UV pulses of several hundred nJ [123]. The use of a Ti:sapphire amplifier is necessary to achieve this level of UV pulse energy; although a Yb-based laser is also an attractive alternative choice [124,125], the long lasing wavelength of Yb is disadvantageous for the construction of a deep UV laser system for our TRPES. Thus, we use a 100 kHz Ti:sapphire regenerative amplifier. The schematic diagram of the system is shown in Figure 9.

The system starts from a cryogenically cooled Ti:sapphire regenerative amplifier that delivers 80 fs pulses at 800 nm with the pulse energy of 70 μJ at 100 kHz. A part of the fundamental beam is focused onto a sapphire plate to generate white light continuum extending from 400 to 650 nm. The main fundamental beam is gently focused onto a β-barium borate crystal to generate the second harmonic. A small portion (5 μJ) of the 400 nm beam is sent to a deep UV frequency-conversion setup, while the main part (28 μJ) is used to pump non-collinear optical parametric amplifier (NOPA) [126–129]. The pulse

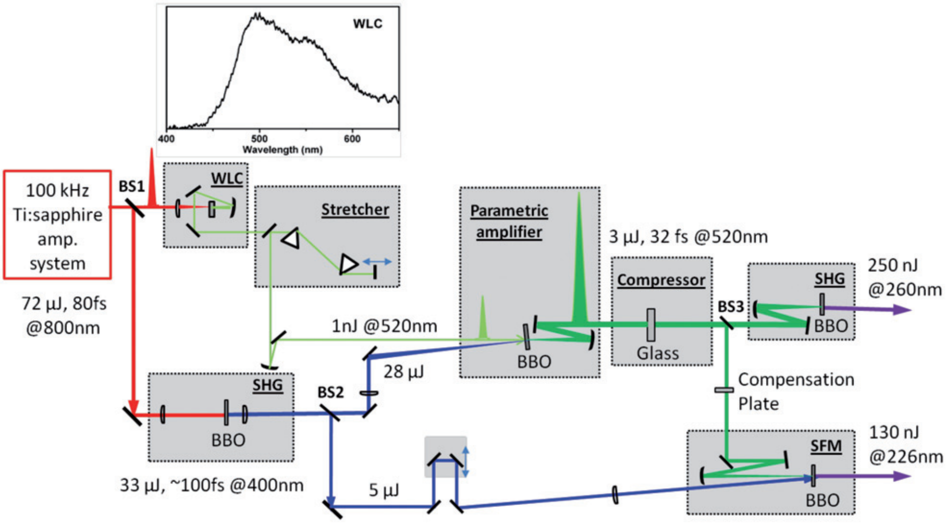

Figure 9. (Colour online) Experimental setup of high-repetition-rate sub-40 fs deep UV laser system. The inset shows the measured spectrum of white light continuum. Reproduced with permission from Ref. [123] (Copyright 2011 The Optical Society).

duration of the white light continuum is stretched by a fused-silica prism pair and used as a seed pulse for NOPA. The pump and seed pulses are focused onto a β-barium borate (type-I) crystal to amplify the seed pulse up to 3.0 μJ. Because only a part of the seed pulse temporally overlaps with the 400 nm pulse in the crystal, the desired bandwidth and centre wavelength can be selected by fine-tuning the chirp and delay of the seed pulse. The negative chirp of the signal pulse from the NOPA, originating from the stretcher, is compensated by a piece of glass: the duration of the compressed pulse is 34 fs. The NOPA output is divided into two parts: the transmitted beam is converted to the second harmonic (260 nm), while the reflected one is mixed with 400 nm to generate 226 nm. The generated deep UV pulse energies are 250 nJ at 260 nm and 130 nJ at 226 nm. Their power drifts are within 2% rms. The spectra of the 226 and 260 nm pulses support the transform-limited pulse width of 38 and 37 fs, respectively.

5. Gas phase dynamics: time–energy mapping of anisotropy parameters

5.1. *Pyrazine: ultrafast internal conversion via conical intersection*

The $S_2(^1B_{2u}, \pi\pi^*)$–$S_1(^1B_{3u}, n\pi^*)$ internal conversion of pyrazine ($C_4H_4N_2$, D_{2h}) is a classic example of ultrafast electronic deactivation. The low-lying conical intersection between S_2 and S_1 potential energy surfaces was identified as the origin of ultrafast internal conversion in 1988 [130]; thereafter, the topography of the conical intersection between the two states was extensively studied by *ab initio* calculations [131–144]. Although pyrazine has 24 normal modes, only a single mode Q_{10a} (b_{1g}) mediates the S_2–S_1 coupling, and a few totally symmetric (a_g) modes play principal roles in vibrational dynamics. This simplicity, despite the large size of this molecule, makes pyrazine a benchmark for theoretical studies

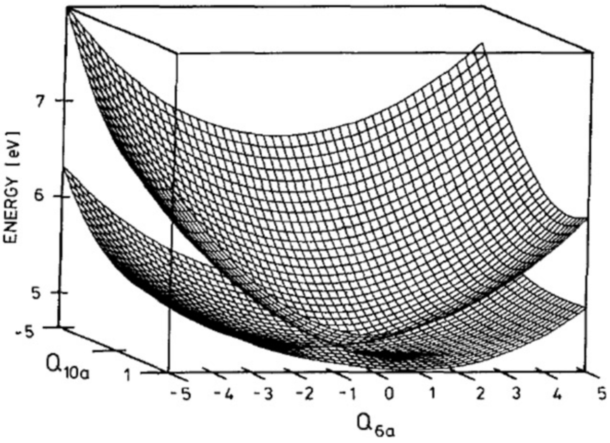

Figure 10. Conical intersection of S_2 and S_1 adiabatic potential energy surfaces of pyrazine in the two-dimensional space spanned by Q_{10a} and Q_{6a}. Reproduced with permission from Ref. [132] (Copyright 1994 American Institute of Physics).

on ultrafast internal conversion through conical intersections. The conical intersection is depicted in Figure 10 for two-dimensional space of Q_{10a} and Q_{6a}.

The $S_2 \leftarrow S_0$ photoabsorption spectrum is well reproduced by *ab initio* calculations. Since the absorption spectrum is the Fourier transform of the autocorrelation function of a wave packet prepared by photoexcitation [145,146], the spectrum provides information on ultrafast dynamics. It is, however, a rather limited view of the dynamics through the observation window in the Franck–Condon region.

TRPES enables exploration of wave packet dynamics in wider regions of the S_2 and S_1 potential energy surfaces, including the conical intersection. A pump pulse creates a wave packet on the S_2 potential energy surface, and a time-delayed probe pulse interrogates the time-evolving wave packets by projecting the non-stationary wavefunction to the $D_0(^2A_g, n^{-1})$ and $D_1(^2B_{1g}, \pi^{-1})$ states of the cation. TRPES of pyrazine was proposed by Seel and Domcke [147], using model calculations taking into account three vibrational coordinates of Q_1, Q_{6a}, and Q_{10a}. The calculations, assuming a hypothetical pump pulse of 1 fs full width at half maximum and a 16 fs probe pulse, demonstrated observation of an oscillating wave packet motion between the ($\pi\pi$*) and ($n\pi$*) electronic characters. Hahn and Stock [148] have performed similar simulations by including Q_{9a} in the calculations.

We have performed our first TRPEI of pyrazine in 1998; the time-resolution (450 fs), however, was insufficient for observing the ultrafast decay of S_2 pyrazine, and only the S_1 decay ($\tau \sim 20$ ps) after S_2–S_1 internal conversion was observed [115,116]. A similar study by Stert *et al.* [149] was still unable to observe ultrafast wave packet dynamics. Since the Franck–Condon region in the S_2 state of pyrazine is close to the S_2/S_1 minimum energy conical intersection point, the internal conversion occurs within a fraction of a vibrational period (<30 fs). The difficulty in generation of sub-30 fs deep UV pulses has impeded TRPES of pyrazine for many years. By constructing the sub-20 fs deep UV laser described

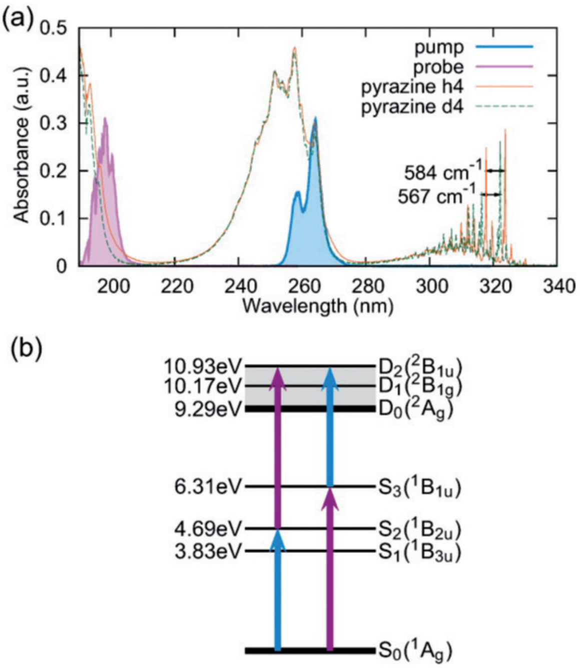

Figure 11. UV photoabsorption spectra of: (a) S_1, S_2 and S_3 of pyrazine-h4 (thin solid line) and pyrazine-d4 (thin dashed line) at room temperature. The spectra of our pump (264 nm, 4.70 eV) and probe (198 nm, 6.26 eV) pulses are also shown in solid lines and (b) schematic energy diagram of pyrazine. Adapted with permission from Ref. [150] (Copyright 2010 Amercian Institute of Physics).

in Section 4.2, we have succeeded in resolving S_2–S_1 dynamics of pyrazine through TRPEI in 2010 [114].

Figure 11(a) shows the UV photoabsorption spectra of pyrazine (pyrazine-h4) and fully deuterated pyrazine (pyrazine-d4) vapour measured at room temperature. Overlaid are the spectra of our pump (264 nm: blue) and probe (198 nm: red) pulses. The pump pulse overlaps with the S_2–S_0 band near the origin, while the probe pulse overlaps (unfavourably) with the S_3–S_0 band slightly. Figure 11(b) shows a schematic energy diagram of our experiment. The sum of the photon energies of the pump (4.70 eV) and probe (6.26 eV) pulses is 10.96 eV, which makes ionisation to the three ion states of D_0, D_1 and D_2 energetically possible.

Figure 12(b) shows the pump–probe photoelectron signal, for pyrazine-h4, that corresponds to the integrated value of $\sigma(E, t)$ over energy, $I(t) = \int_0^\infty \sigma(E, t)\mathrm{d}E$. The signal rapidly decays within the first 100 fs and exhibits a plateau at later times: previous experiments have shown that this long-lived component has a finite lifetime of 22 ps for pyrazine-h4 [115,149]. The observed time profiles can be explained by three components: an exponential decay, a corresponding exponential rise in the positive time range, and an exponential decay in the negative time range. The three components correspond to the decay of optically excited S_2 (red), the corresponding growth of S_1 (blue) populated by

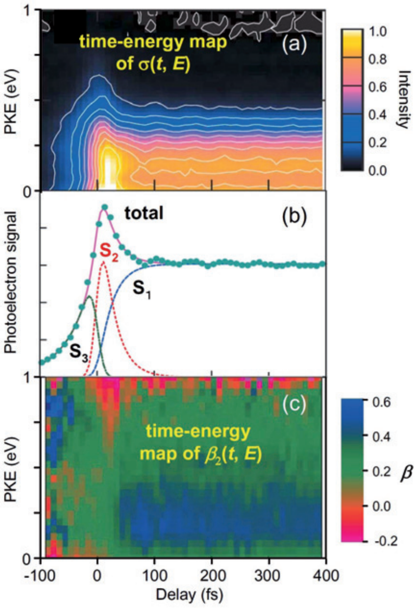

Figure 12. (a) Time-evolution of photoelectron kinetic energy distribution, $\sigma(E, t)$ and (b) temporal profiles of total photoelectron signals in $(1+1')$ TRPEI of pyrazine-h4. The observed data are well explained by three components: single-exponential decay of S_2 (red); corresponding increase in S_1 (blue) in the positive time delay and single-exponential decay of S_3 (green) in the negative-time delay. The fitting result is shown as a solid line. (c) Time-evolution of photoelectron angular anisotropy parameter $\beta_2(E, t)$.

internal conversion from S_2, and the decay of S_3 (green), respectively. The last component arises from the reverse process: 198 nm pump and 264 nm probe. By the least squares fitting, the $S_2 \rightarrow S_1$ internal conversion time constants are estimated as 23 ± 4 fs for pyrazine-h4 and 20 ± 2 fs for pyrazine-d4. The time constants for S_3 decay were 43 ± 3 fs for pyrazine-h4 and 44 ± 3 fs for pyrazine-d4. The plateau region exhibits oscillatory features due to vibrational quantum beats. Fourier transform of this feature ($t > 50$ fs) exhibits a frequency component of $560 \pm 40\,\mathrm{cm}^{-1}$, which agrees with the vibrational frequency of Q_{6a} in S_1 ($583\,\mathrm{cm}^{-1}$). Similarly, pyrazine-d4 exhibited a Fourier component of $550 \pm 40\,\mathrm{cm}^{-1}$, which further confirms the assignment to Q_{6a} ($\nu_{6a}(S_1) = 564\,\mathrm{cm}^{-1}$ for pyrazine-d4) [151].

Figure 12(a) shows a time–energy map of $\sigma(E, t)$. From the analysis of photoelectron intensity in Figure 12(b), the $S_2 \rightarrow S_1$ internal conversion must be occurring within 30 fs; no marked change is seen, however, in $\sigma(E, t)$. This is understood based on the one-electron model of photoionisation, shown in Figure 13. Because of the electron configurations, photoionisation predominantly occurs as $D_0(n^{-1}) \leftarrow S_1(n\pi^*)$ and $D_1(\pi^{-1}) \leftarrow S_2(\pi\pi^*)$ and the energy differences are almost identical between D_1 and D_0 (0.88 eV) [117] and between S_2 and S_1 (0.86 eV) [152]. Therefore, $\sigma(E, t)$ exhibits almost no change upon internal conversion.

PAD is the key observable in photoelectron imaging. Figures 12(c) shows the time–energy map of $\beta_2(E, t)$; the positive (blue–green) and negative (red) values correspond to

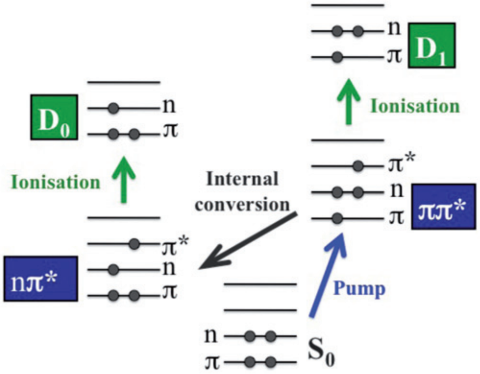

Figure 13. (Colour online) Photoionisation schemes of pyrazine within the framework of the frozen-core approximation.

preferential ejection of an electron parallel and perpendicular to the probe laser polarisation (Equation (1)). The energy-dependence of β_2, a stripe of colours at each time delay in Figure 12(b), is the fingerprint of the electronic character. The map clearly shows that there are three different components, one in the negative time and two in the positive time, in agreement with the analysis of $\sigma(E, t)$. The most distinct feature is the sudden change of the colour at *ca* 30 fs that is attributed to ultrafast $S_2 \rightarrow S_1$ internal conversion. $\beta_2(E, t)$ does not change after 30 fs, indicating that the electronic character remains $(n\pi^*)$; no revival of the $(\pi\pi^*)$ character is identified. This may be ascribed to our photoexcitation of pyrazine near the S_2 origin, because if the energy flows into various modes of S_1 the wave packet has no chance to return to the Franck–Condon region. Photoexcitation to higher vibronic levels in S_2 may enable recurrence of the $(\pi\pi^*)$ character.

Werner *et al*. [78] have performed theoretical simulations of TRPES of pyrazine using molecular dynamics on the fly. They have taken into account all vibrational modes and calculated their classical trajectories using the gradients of electronic energies (on the fly) obtained by time-dependent density functional theory. Non-adiabatic transitions were taken into account using Tully's [153] fewest switches algorithm. The photoionisation cross sections were calculated using Stieltjes imaging (or Stieltjes–Chebyshev moment theory approach) with the computational procedure suggested by Gokhberg *et al*. [154]. As seen in Figure 14, the calculated kinetic energy distribution is in good agreement with experimental result.

Very recently, Lin *et al*. [144] suggested that the ^1A_u and $^1B_{2g}$ states are located between $^1B_{2u}$ and $^1B_{3u}$ and are involved in deactivation process of the $^1B_{2u}$ state, based on complete active space second order perturbation theory. So far, no clear experimental evidence has been reported for a possible role of ^1A_u in internal conversion from the $^1B_{2u}$ state.

5.2. *Benzene and toluene: variation of electronic character along reaction path*

Benzene is a prototypical aromatic molecule and considered a benchmark for theoretical and experimental studies of organic compounds. The lifetime of the $S_1(^1B_{2u})$ state of

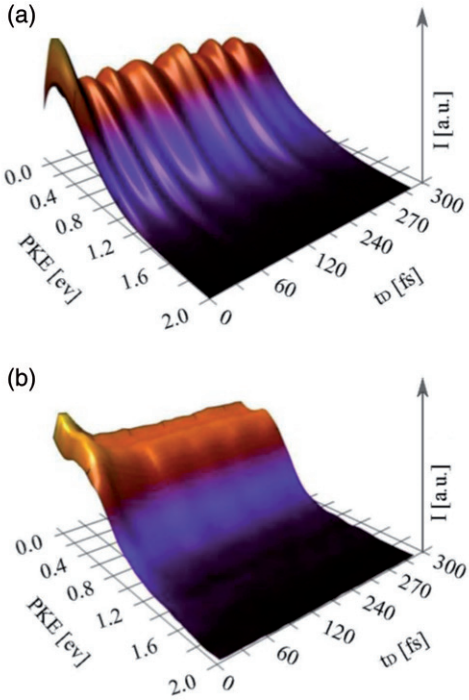

Figure 14. Time-dependent photoelectron kinetic energy distribution in TRPES of pyrazine: (a) theoretical simulation using molecular dynamics on the fly and Stielejes imaging and (b) experimental result.

benzene is 50–100 ns near the origin [155,156], while the $S_2(^1B_{1u})$ lifetime is much shorter (<100 fs) owing to ultrafast S_2–S_1 internal conversion. Similar to the case of pyrazine, the ultrashort S_2 lifetime implies that photoexcited benzene easily accesses an S_2/S_1 conical intersection region. In fact, theoretical calculations predicted that the minimum energy S_2/S_1 conical intersection point (a prefulvenic form) is close, in energy and structure, to the S_2 potential minimum [98,157,158]. The minimum, however, is at a non-planar structure (a boat form) that differs from the planar structure of benzene ($D_{6\mathrm{h}}$) in S_0 [98,157,158]. Consequently, a photoexcited benzene molecule rapidly deforms from a planar structure in the Franck–Condon region towards a non-planar structure along the steepest descent of the S_2 potential energy surface and undergoes a non-adiabatic transition in the vicinity of the S_2/S_1 seam of crossings. This is a different feature from the pyrazine case in which the Franck–Condon region is close to the minimum energy conical intersection point. The hot S_1 benzene produced by S_2–S_1 internal conversion is further funnelled down to S_0 via S_1/S_0 conical intersection in <10 ps [158–160]. These features of the photophysical properties of benzene are also seen for benzene derivatives: the lifetimes of S_2 and hot S_1 have been reported as 50 ± 10 fs and 4.3 ± 0.2 ps for toluene [161], 43–54 fs and 9.4–88 ps for indene, styrene and phenylacetylene [162], and 60 fs and 9.9 ps for *o*-xylene [163].

We have performed TRPEI of benzene and toluene using a 198 nm pump pulse (17 fs) and a 264 nm probe pulse (14 fs) [164]. Figure 15(a) and (b) shows the time profiles of the photoionisation signal intensity observed for benzene and toluene, respectively. The time profiles of the electron (circles) and ion (triangles) signals are in excellent agreement with each other: both exhibit a fast decay. The broken lines are the best-fit single exponential decay function convoluted with the cross-correlation of the pump and probe pulses (Gaussian with a full width at half maximum of 22 fs). The effective lifetime thus estimated for benzene and toluene were, respectively, 48 ± 4 and 62 ± 4 fs, which are in excellent agreement with 40 ± 10 and 50 ± 10 fs estimated by Radloff *et al.* using much longer pulses (>100 fs) [159,161]. Close examination of our experimental results, however, reveals that a single exponential decay model does not adequately reproduce the observed time profiles in either case. The observed non-exponential profiles are, in fact, reproduced better by assuming molecular response functions shown in Figure 16: the flat part of the response function corresponds to propagation of a wave packet from the Franck–Condon region to the seam of crossings during which time no population decay occurs from S_2. The arrival times of the wave packets at the seam of crossings are estimated as 33 fs for benzene and 41 fs for toluene: the subsequent decay time is 32 fs for benzene and 43 fs for toluene. The longer time observed for toluene may be ascribed to a larger inertia for the out-of-plane vibration. The existence of these lag times was identified for the first time by TRPES experiments with the time resolution of 22 fs.

The movies of time-evolving photoelectron images (slices through three-dimensional velocity distribution) are available as supplementary materials for the original paper [164]. The photoelectron kinetic energy distributions at each time delay, $\sigma(E, t)$, are extracted from the movies as shown in Figure 15(c) and (d) for benzene and toluene, respectively. The distributions consist of the S_2 and S_1 components that are largely different each other. The S_2 component mainly appears in 0–1.5 eV, while $S_1 < 0.3$ eV: the difference of kinetic energies originate from the fact that the electronic energy difference between S_2 and S_1 is transformed into the vibrational energy in S_1, and the vibrational energy is approximately conserved upon ionisation [159,160,164]. Since our probe photon energy is insufficient to cover the entire Franck–Condon envelope in ionisation from S_1, the quantum yield of S_2–S_1 internal conversion cannot be evaluated accurately from our result.

For both benzene and toluene, close examination of the high-energy (1–1.5 eV) region of the S_2 component reveals vibrational wave packet dynamics. The molecules are planar in the Franck–Condon region of S_2, and therefore, ionisation at $t = 0$ occurs to low vibrational levels of the cation, which also has a planar structure. As the vibrational wave packet moves out from the Franck–Condon region, ionisation starts occurring to vibrationally excited states of the cation, lowering the entire distribution in energy from the moment the photoelectron signal initially appears. Another interesting feature is an oscillatory component that appears as a red triangular shape in Figure 15(c) and a red–yellow region in Figure 15(d). Fourier analysis reveals that the oscillatory component has a time period of 20 fs in Figure 15(c) and 24 fs in Figure 15(d), respectively. If they correspond to vibrational periods, the vibrational frequency will be *ca* 1700 and 1400 cm^{-1}, respectively [164]. However, the experimental and theoretical S_2–S_0 absorption spectra revealed progressions of the totally symmetric ring-breathing mode Q_1 whose fundamental frequencies are 993 and 785 cm^{-1} in benzene and toluene in S_0, respectively. Thus, interpretation of these wave packet dynamics is not established yet: measurements in

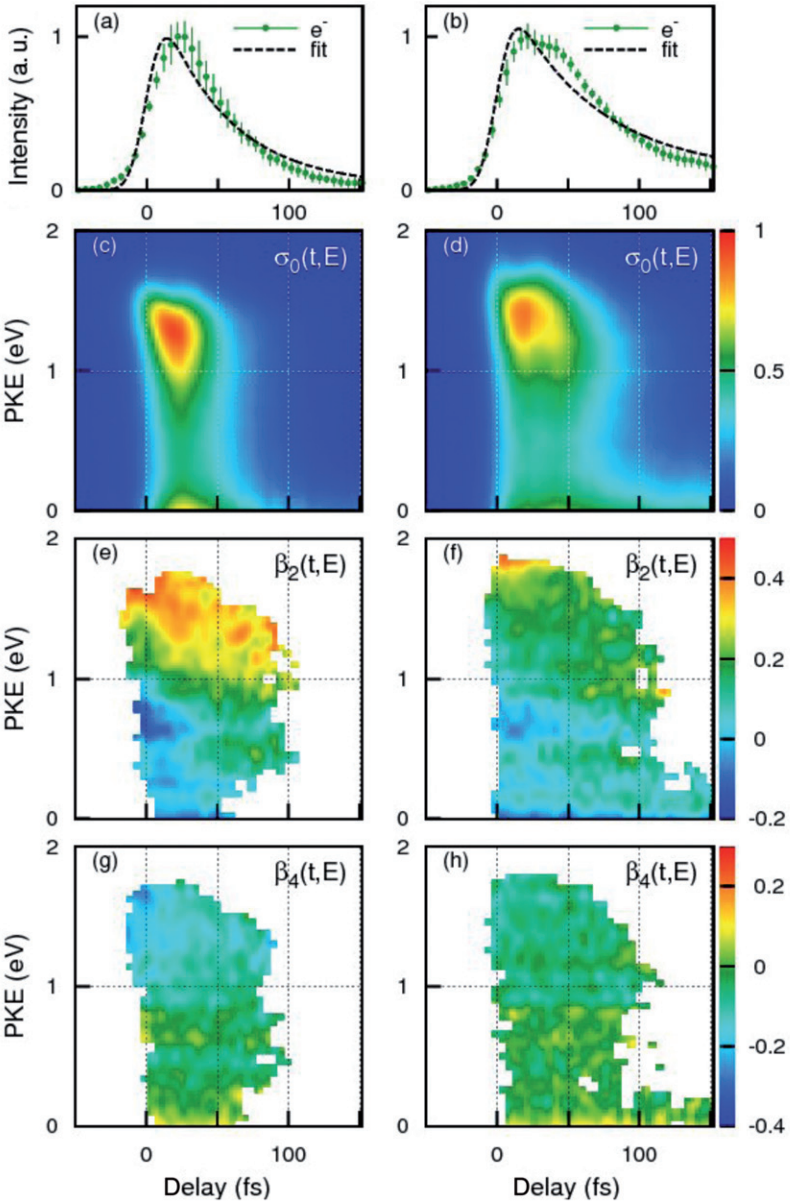

Figure 15. The time profiles of the photoionisation signal intensity for: (a) benzene and (b) toluene. Photoelectron signals are indicated by green dots with error bars. Time–energy maps of the photoelectron intensity, $\sigma(E, t)$, for: (c) benzene and (d) toluene. Time–energy maps of the photoelectron angular anisotropies, $\beta_2(E, t)$, for: (e) benzene and (f) toluene and $\beta_4(E, t)$ for: (g) benzene and (h) toluene. Data points for β_2 and β_4 with standard deviations smaller than 0.2 are shown (see text). Adapted with permission from Ref. [164] (Copyright 2011 American Institute of Physics).

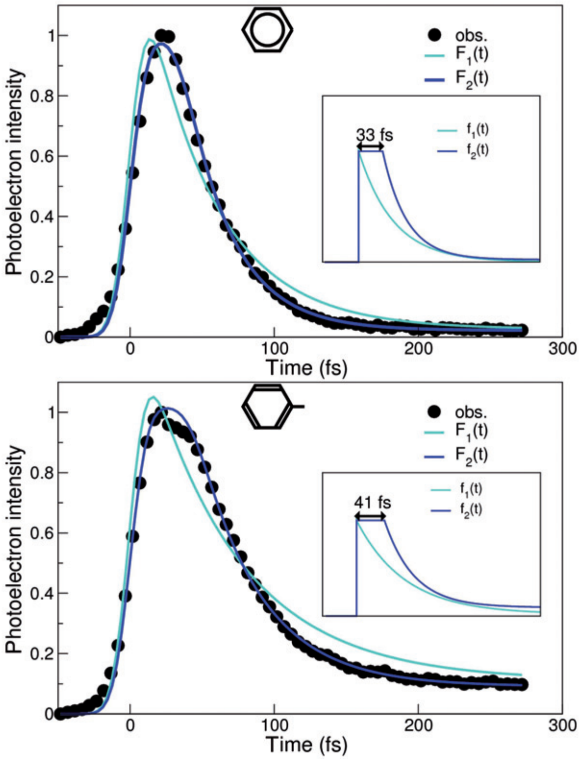

Figure 16. (Colour online) Analysis of photoionisation time profiles assuming lag times prior to population decay for benzene and toluene. The dots are the experimental data points. Light-blue solid lines are the least squares fitting assuming an exponential decay from the S_2 state, while blue solid lines are assuming a lag time prior to the exponential decay. The insets show the molecular response functions assumed in the analysis, and the solid lines in the main panels were obtained by convoluting them with an apparatus function of a Gaussian with FWHM of 22 fs.

higher resolution and theoretical simulation of multi-dimensional vibrational dynamics are necessary.

Close examination of Figure 15(e) for benzene reveals that β_2 varies with time, most clearly around 0.7 eV; β_2 is negative at $t = 0$ and gradually increases with time to be positive around *ca* 30 fs. Similar time dependence of β_2 is also seen in Figure 15(f) for toluene, for example at around 1.0 eV. These rapid changes of $\beta_2(E, t)$ with time indicate variation of the electronic character along the out-of-plane distortion. The variation is most likely due to mixing of the $^1E_{1u}$ and/or $^1E_{2g}$ characters into the S_2 state. In consideration of the possible roles of these two electronic states, it is important to note that the photoionisation cross section does not vary largely in the first 20 fs (Figure 16). Since photoionisation from $^1E_{2g}$ to $D_0(\mathrm{e}_{1\mathrm{g}}^{-1})$ is forbidden within the frozen-core approximation while $^1E_{1u}$ has a similar integral cross section with that of $^1B_{1u}$, the observed rapid change of $\beta_2(E, t)$ at short time delay is ascribed to mixing of the $^1E_{1u}$ character into $^1B_{1u}$. Meisl and Janoschek [157] and Palmer *et al.* [98] studied the minimum

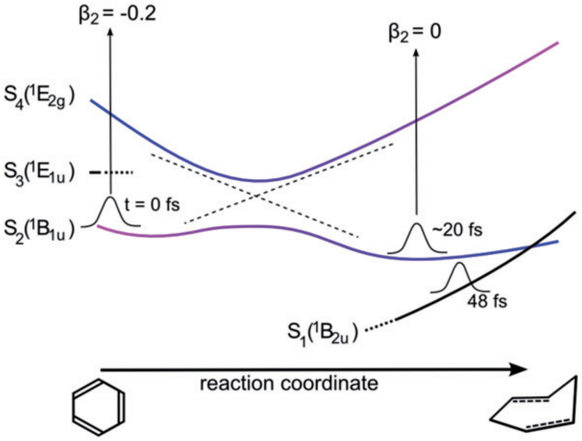

Figure 17. (Colour online) Schematic potential energy curves of benzene along the reaction coordinate from the D_{6h} equilibrium geometry (Kekulé benzene) to the S_2–S_1 minimum energy conical intersection point (prefulvenic form). The figure was drawn by considering the avoided crossing (dashed lines) between S_2 ($^1B_{1u}$) and S_4 ($^1E_{2g}$) reported by Meisl and Janoschek [157]. Reprinted with permission from Ref. [164] (Copyright 2011 American Institute of Physics).

energy region of the adiabatic S_2 PES and suggested that the electronic character of the $^1E_{2g}$ state mixes into S_2 in that region. The mixing of these electronic states and symmetry lowering from the planar to non-planar geometry are closely coupled to each other (Figure 17).

5.3. *Furan: elucidation of deactivation pathway*

Furan (C_4H_4O, C_{2v}) is a fundamental heterocyclic aromatic molecule that serves as a structural unit in various biological substances. This molecule exhibits a broad UV absorption spectrum that has been ascribed to four electronic transitions to the $^1A_2(\pi 3s)$, $^1B_2(\pi\pi^*)$, $^1A_1(\pi\pi^*)$, and $^1B_1(\pi 3p_y)$ states, in which the transition to $^1A_2$ is weakly allowed by vibronic coupling with $^1B_2$. Figure 18 shows the absorption spectrum at room temperature and the corresponding theoretical spectrum calculated by time-dependent density functional theory. The strong absorption feature at <6 eV is due to the $S_2 \leftarrow S_0$ transition, and the weak feature in the low energy part (5.6–6.0 eV) is $S_1 \leftarrow S_0$ [166–171]. Another strong transition of $^1B_1(\pi 3p_y) \leftarrow S_0$ is at 6.45 eV and outside of our pump spectrum. Photophysics of furan has been studied by multiconfigurational time-dependent Hartree wave packet calculations with the potential energy surfaces determined by *ab initio* equation-of-motion coupled cluster method [172]. The calculations predict that the $^1B_2(\pi\pi^*)$ state undergoes ultrafast internal conversion to $^1A_2(\pi 3s)$ within <25 fs through a conical intersection, while the lifetime of $^1A_2(\pi 3s)$ is longer than 200 fs. The conical intersection with S_0, however, was not considered in these calculations. Another theoretical study, using a combined density functional/multireference configuration interaction method, suggested that molecules excited to the $^1B_2(\pi\pi^*)$ state undergo a ring-opening reaction via the $^1B_1(\pi\sigma^*)$ state [173].

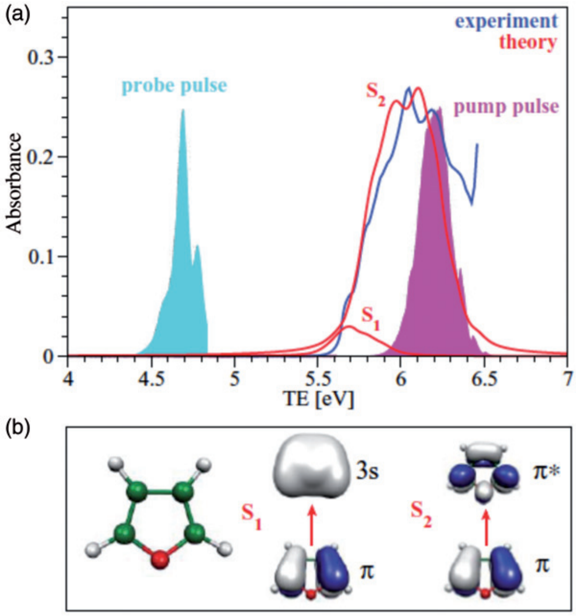

Figure 18. (Colour online) (a) Absorption spectrum (blue) of furan at room temperature and theoretical spectrum (red) for $S_1(^1A_2(\pi 3s))$ and $S_2(^1B_2(\pi\pi^*))$ states at $T = 300\,K$. The discrete absorption lines for each member of the ensemble were convoluted with a Lorentzian function with a width of 0.1 eV and added together. The spectra of our pump (6.2 eV, 198 nm) and probe (4.7 eV, 264 nm) pulses are shown as filled curves. (b) Equilibrium structure of furan in the neutral ground state with character of the $S_1(\pi 3s)$ and $S_2(\pi\pi^*)$ transitions. Adapted with permission from Ref. [165] (Copyright 2010 American Institute of Physics).

We studied excited-state dynamics of furan by TRPEI and molecular dynamics on the fly. The observed time profiles of photoion and photoelectron signals are shown in Figure 19(a). The least squares fitting assuming a single exponential function (green solid line in Figure 19(a)) provides the lifetime of the excited state as 46 fs; the single exponential decay, however, does not provide an adequate fit of the time profile, as in the case of benzene and toluene. For comparison, a time profile extracted for the specific kinetic energy of 1.6 eV is well reproduced by a single exponential function, as shown in a solid line in Figure 19(b). The signal in Figure 19(b) appears immediately at the time origin, indicating that this state is directly photoexcited from S_0: the lifetime of this state is 29 fs.

The false colour pictures in Figure 20 are the two-dimensional slices through three-dimensional photoelectron velocity distributions measured at some selected pump-probe time delays: the sliced plane involves the polarisation axis of the lasers in the vertical direction in the figure. The movie of time-evolving photoelectron image is available as a supplementary material of the original paper [165]. Examination of Figure 20 reveals that a sharp ring in the outer part of the image disappears rapidly within 50 fs. Careful inspection of the image confirms that this ring is anisotropic: a larger number of electrons are ejected in the vertical than horizontal direction. This narrow speed distribution with strong angular anisotropy is the fingerprint of photoionisation from a Rydberg state: the

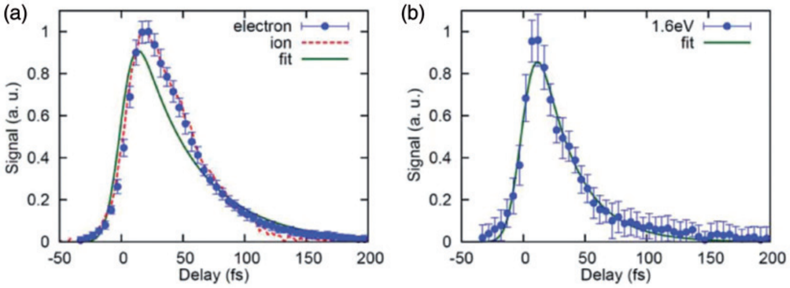

Figure 19. (Colour online) (a) Temporal profiles of total photoelectron (solid circles) and photoion (dotted line) signal in $(1+1')$ TRPEI of furan. The result of least squares fitting with a single exponential decay $[\exp(-t/\tau)]$ convoluted with our apparatus function (Gaussian with 22 fs FWHM) is also shown as a solid line ($\tau = 46.3$ fs). (b) Temporal profile of photoelectron intensity at photoelectron kinetic energy of 1.6 eV. The result of least square fitting with a single exponential decay convoluted with the apparatus function is shown as a solid line ($\tau = 29.0$ fs). Reprinted with permission from Ref. [165] (Copyright 2010 American Institute of Physics).

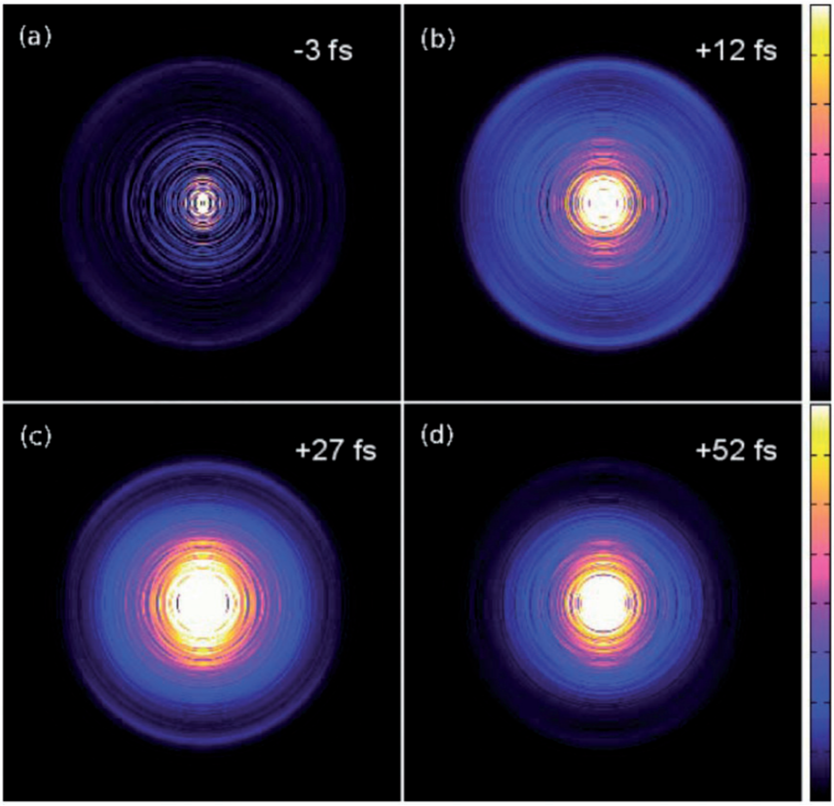

Figure 20. False-colour presentation of furan photoelectron images observed at different pump–probe time delays of (a) −3 fs, (b) 12 fs, (c) 27 fs and (d) 52 fs. The images correspond to the two-dimensional slices of three-dimensional distributions calculated by the pBasex method. Reproduced with permission from Ref. [165] (Copyright 2010 American Institute of Physics).

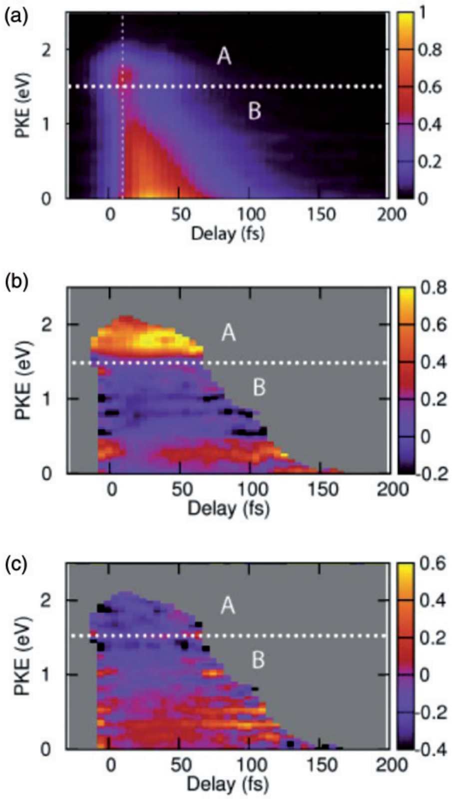

Figure 21. Two-dimensional maps obtained from TRPEI of furan. (a) Time evolution of $\sigma(E, t)$. The vertical dotted line is at delay time of 10 fs, where the temporal peaks of high-energy components appear. The high and low energy components, separated by horizontal lines, were denoted by A and B, respectively. Time-dependent photoelectron anisotropy parameters: (b) $\beta_2(E, t)$ and (c) $\beta_4(E, t)$ extracted from observed photoelectron images of furan. The gray area corresponds to where the intensity is lower than 0.05 in (a). The β_2 and β_4 values in this area are not reliable since the intensity of the signal is low. Reprinted with permission from Ref. [165] (Copyright 2010 American Institute of Physics).

narrow distribution arises from the $\Delta v = 0$ propensity rule (v: vibrational quantum) owing to very similar potentials of a Rydberg state and cation, and strong anisotropy originates from an atomic like Rydberg orbital. This ring is at the kinetic energy of 1.6 eV. Thus, it is concluded that the 1.6 eV signal is due to photoionisation from S_1 (3s Rydberg).

The time–energy maps of $\sigma(E, t)$, $\beta_2(E, t)$ and $\beta_4(E, t)$ are shown in Figure 21. Each map can be separated into regions of $E > 1.5$ eV (region A) and 0.0–1.5 eV (region B). The former exhibits high β_2 values (<0.8) that are typical of photoionisation from a 3s Rydberg state. The kinetic energy 1.6 eV is smaller by 0.4 eV than the maximum possible energy of 2.0 eV, which is consistent with the estimated vibrational energy in S_1, ca. 0.3–0.4 eV [174]. The region B exhibits a broad $\sigma(E, t)$ and low β_2, which indicates ionisation from a valence state $^1B_2(\pi\pi^*)$. The intensity maxima of $\sigma(E, t)$ in the region B are systematically time-delayed for lower energy. The lag time is ascribed to a vibrational

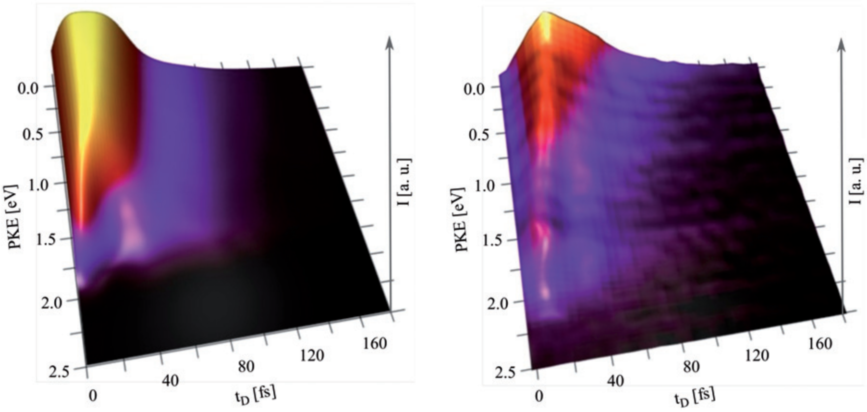

Figure 22. (Colour online) Comparison of theoretical (left) and experimental $\sigma(E, t)$ for furan.

wave packet motion from the Franck–Condon region to the molecular structure monitored with particular photoelectron kinetic energy. The results suggest that the molecules photoexcited to $^1B_2(\pi\pi^*)$ undergo large structural deformation within 50 fs, and that they do not undergo efficient internal conversion to $^1A_2(\pi 3s)$, contradicting with the theoretical prediction previously made [171,172].

In order to interpret our experimental results, we performed molecular dynamics on the fly with time-dependent density functional theory for electronic structure calculations: we confirmed that the calculated sections of the potential energy surfaces are in good agreement between time-dependent density functional theory and equation-of-motion coupled cluster method. The observed and calculated $\sigma(E, t)$, shown in Figure 22, are in reasonable agreement, suggesting the validity of our theoretical treatments. Figure 23 shows the electronic energy of the system in one selected trajectory: the black, red, green and blue lines indicate electronic energies of the S_0–S_3 adiabatic states along this trajectory, respectively. The photoexcited molecule rapidly changes from the adiabatic S_2 to S_1 state in the first ~10 fs: the system, however, preserves the $\pi\pi^*$ character. In other word, the system evolves diabatically in the $\pi\pi^*$ state up to 70 fs.

Very recently, Gromov *et al*. have investigated the ring-opening reaction of furan from the first two excited singlet states [175]. From experimental point of view, TRPES using vacuum UV radiation is indispensable for elucidating the dynamics involving internal conversion to S_0 and ring-opening reactions.

5.4. *TRPES using vacuum UV radiation*

A useful case study for the importance of vacuum UV radiation in TRPES is offered by previous studies on photophysics of DNA bases. It has been suggested that nature's selection of adenine, thymine, guanine and cytosine as carriers of genetic information is based on photostability. The stability is closely related to ultrafast internal conversion mechanism that releases electronic excitation energy as heat to the surrounding bath in the condensed phase and prevents photochemical reactions [176–178]. Given this supposition,

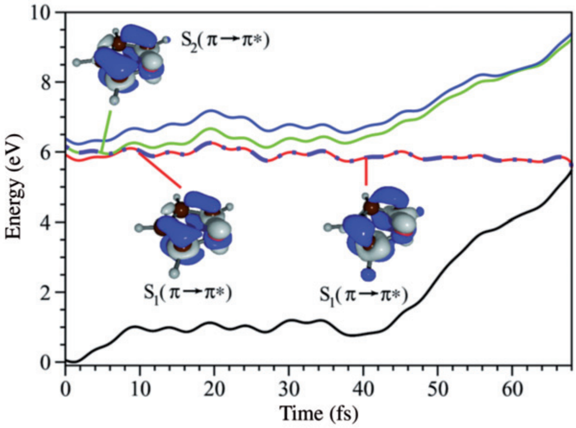

Figure 23. (a) Electronic energies of S_0 (black) and three excited states (red S_1, green S_2 and blue S_3) of furan as a function of time along one selected nuclear trajectory in non-adiabatic dynamic calculations. The notations of the electronic states are for adiabatic states. The populated state during the dynamics, indicated with a dashed violet line, is initially S_2 but after ca. 10 fs changes to S_1. The orbital character of the HOMO indicated as insets, however, is always of π^*. Thus, the system is evolving along a diabatic pathway up to 70 fs. Reprinted with permission from Ref. [165] (Copyright 2010 American Institute of Physics).

one can ask whether ultrafast internal conversion is an inherent property of the isolated molecules of DNA bases or induced by the environment. Thus, several research groups have investigated the lifetime of excited electronic states of DNA bases. Three different pump–probe photoionisation experiments were performed using the $(\omega_{267}+3\times\omega_{800})$ [179], $(\omega_{267}+2\times\omega_{400})$ [180], and $(\omega_{267}+\omega_{200})$ [181] ionisation schemes: the subscripts are the wavelength in nm. All of these experiments have found ultrafast decay, typically biexponential, of the photoionisation signal. Some groups have interpreted the fastest decay (<100 fs) as internal conversion. Martinez and coworkers, however, have shown theoretically that the photoexcited uracil and thymine undergo wave packet motion towards a non-planar S_2 minimum in sub-ps, which rapidly increases vertical photoionisation energy and substantially decreases the signal (Figure 24) [182]. Thus, they suggested the fastest decay component is due to vibrational dynamics and not internal conversion. TRPES using a vacuum UV or extreme UV lasers is expected to be useful for studying these problems more clearly, although the use of short wavelength laser brings its own technical difficulties.

At present, femtosecond pulses in the vacuum UV and extreme UV region can be generated by at least three different ways, high harmonic generation using an intense femtosecond laser [7,183,184], a free electron laser [185–187], and four-wave mixing [107,188–191]. Liu *et al.* [192] performed the first TRPEI experiment using a vacuum UV free electron laser (SCSS: SPring-8 Compact SASE Source) [186] synchronised with a femtosecond UV laer. Although SCSS is normally operated at 60 nm, the 60 nm photon ionises the ground state molecules and decreases the one- and two-colour signal ratios. Therefore, the free electron laser was operated at 161 nm [192], which does not ionise a target molecule from the ground state by one-photon absorption.

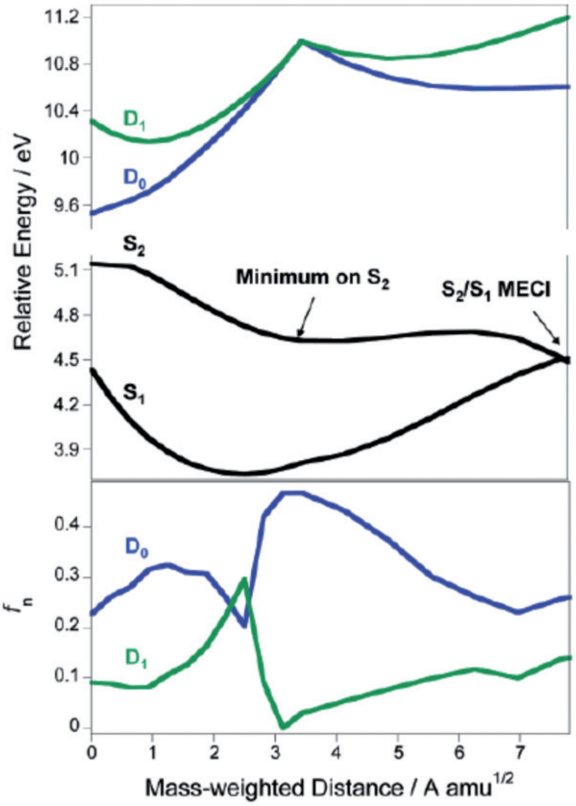

Figure 24. (Colour online) Reaction pathway along S_2, as probed by TRPES. The pathway is determined by linear interpolation in internal coordinates between the S_0 minimum, S_2 minimum, and S_2/S_1 minimum energy conical intersection point. The lowest two cationic states $D_0(\pi^{-1})$ and $D_1(n^{-1})$ are shown along this linear interpolation pathway with their corresponding photoionisation propensities, f_n, (electronic factors). Rapid wave packet motion to the S_2 minimum leads to higher ionisation potentials as well as changes in the photoionisation propensities. In the Franck–Condon region (left side of plot), ionisation to $D_0(\pi^{-1})$ is favoured both energetically and electronically. Reprinted with permission from Ref. [182] (Copyright 2007 American Chemical Society).

Figure 25 compares the photoelectron spectrum measured by 260 nm pump and 161 nm probe of pyrazine (blue curve) and a previous spectrum obtained with a 198 nm probe pulse (red curve) [150]. The latter distribution is truncated at the electron binding energy of 10.96 eV, while 161 nm radiation allows observation of the entire Franck–Condon envelope. The spectra are of photoionisation from the vibrationally excited S_1 state created by ultrafast S_2–S_1 internal conversion. The maximum of the distribution appears in the region corresponding to vibrational energy of ca. 1.2 eV in D_0, which is consistent with the vibrational energy ca. 0.9 eV in S_1. Since S_1 is the $(n\pi^*)$ state and D_0 and D_1 are of n^{-1} and π^{-1}, the frozen-core approximation predicts ionisation occurs from S_1 to D_0, as shown in Figure 13. The experimental result agrees with this picture. Since SCSS uses self amplification of spontaneous emission [186], the vacuum UV pulse

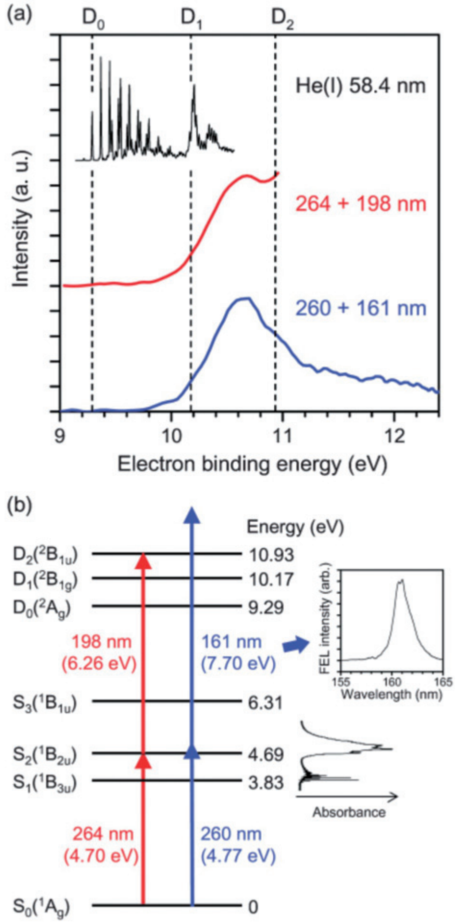

Figure 25. (Colour online) (a) Photoelectron kinetic energy distribution in He(I) photoelectron spectroscopy of the ground-state pyrazine (black) [117], 264 nm pump and 198 nm probe experiment (red) [114] and 260 nm pump and 161 nm probe (blue)[193]. (b) Schematic energy diagram of ionisation process. UV absorption spectrum of pyrazine vapour at room temperature and time-averaged spectrum of VUV FEL are shown as insets. Reprinted with permission from Ref. [193] (Copyright 2010 American Physical Society).

fluctuates in timing and spectrum; the cross-correlation of the pump–probe experiment was *ca* 1 ps and the S_2–S_1 internal conversion could not be observed in real-time using SCSS.

As explained in Section 4.2, filamentation four wave mixing is able to generate 160 nm radiation. For example, we generated 160 nm pulse with the energy higher than 500 nJ at 1 kHz simultaneously with 260 and 200 nm pulses by filamentating four wave mixing of ω and 2ω in Ne. We have also demonstrated generation of 160 nm pulse with the energy over 500 nJ at 1 kHz simultaneously with 200 nm pulse by four-wave mixing of 2ω and 3ω using 80 fs Ti:sapphire laser [188]. These techniques enable performing vacuum UV TRPES using a single filamentaton cell at 1 kHz at a time-resolution superior to 100 fs. When the

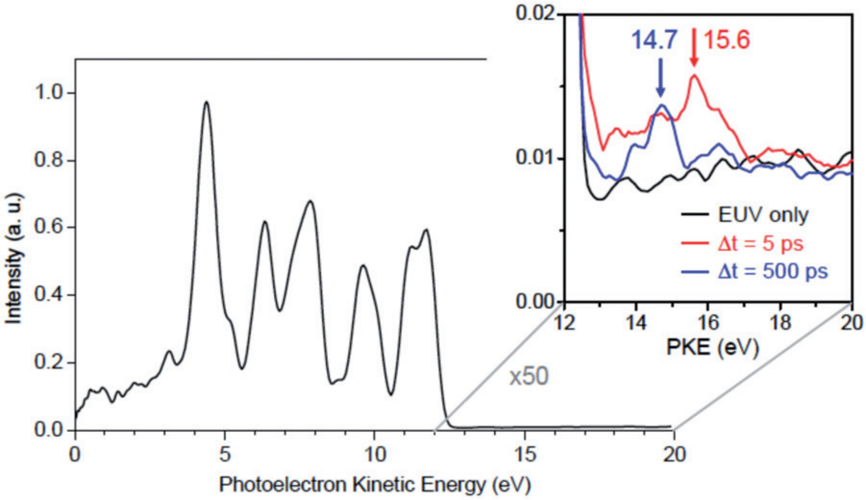

Figure 26. (Colour online) Photoelectron kinetic energy distributions observed by TRPEI of pyrazine using the 324 nm pump and 58.4 nm probe pulses at different time delays. The pump pulse was generated by an UV femtosecond laser, and the probe pulse by SCSS (a vacuum UV free electron laser). Unpublished result [194].

laser pulses are propagated through a vacuum beam line, no compressor is needed. Noack and coworkers have demonstrated the generation of 5ω by four-wave mixing of $3\omega + 3\omega - \omega \rightarrow 5\omega$ [189–191]. Although their method does not produce a deep UV pulse simultaneously with the vacuum UV, sub-20 fs pulse duration has been achieved for 5ω [191]. TRPES experiments using 1 kHz vacuum UV lasers will be highly useful in elucidating photophysics and photochemistry of polyatomic molecules including low-lying excited states and the ground state. The vacuum UV lasers would also allow one-photon ionisation of reaction products and identification of their masses.

A high probe photon energy, which exceeds ionisation energies of the reactants and products, enables ionisation of all chemical species and observation of the entire chemical reaction process by TRPES. It is noted, however, that the high-energy probe photon ionises the ground-state molecules that do not absorb the pump photon, which makes one-colour probe signal considerably stronger than a two-colour pump-probe signal. In these cases, a two-colour signal is observed most clearly in the energy region between $h(\nu_{\mathrm{pump}} + \nu_{\mathrm{probe}}) - IE$ and $h\nu_{\mathrm{probe}} - IE$, because the highest electron kinetic energy of the background signal produced by one-colour photoionisation of the ground-state molecules is $h\nu_{\mathrm{probe}} - IE$. As an example, Figure 26 shows the result of TRPEI of pyrazine using the 324 nm femtosecond laser pulse and the 58.4 nm free electron laser pulse. The UV pump pulse excites pyrazine to the zero vibrational level in $S_1(n\pi^*)$, from which intersystem crossing occurs to $T_1(n\pi^*)$ in 110 ps. The VUV probe pulse can ionise pyrazine from S_0, $S_1(n\pi^*)$, and $T_1(n\pi^*)$; as seen in Figure 26, one-colour photoionisation of ground-state pyrazine is overwhelming. An enlarged view of the high kinetic energy region, however, reveals a two-colour signal appears first from S_1 (red) and then from T_1 (blue) with intensities two orders magnitude smaller than the one-colour signal (black).

6. Liquid phase dynamics: challenge of liquid TRPES

Liquid is the most important phase of matter for material and biological sciences. Although the studies of gas phase reactions elucidate fundamental aspects of chemical reactions, the influence of solvents must be studied in situ in solutions. Solvent effects have been used in chemistry for centuries as a traditional yet robust method to control solution chemistry, and important concepts are well established. For instance, the primary effect arises from electrostatic interactions between a solute and various solvents (or proteins in biological systems) that alter the topography of potential energy (or free energy) surfaces and influences reaction pathways and product yields. Another effect is given by intermolecular collisions and transport phenomena in solution, which are sometimes approximated as friction in intermolecular motions between a solute and solvents [195]. On the other hand, the mechanistic details of individual reactions are not well understood at the molecular level and our ability to predict behaviour of real systems is still low. Aqueous solutions are particularly challenging due to peculiar properties of water, such as the order and disorder of hydrogen-bonding network around a solute. Elucidation of chemical reactions and material transport in aqueous solutions, however, has the paramount importance as the molecular basis of life [196]. Complete explication requires detailed experiments and molecular dynamics simulations using realistic interaction potentials. Such simulations are now becoming more and more feasible and useful in vast area of science and technology. Photochemistry and photophysics of hydrated molecules, however, require not only classical mechanical molecular dynamics simulation but also high-quality quantum mechanical calculations of the reaction centre and consideration of non-adiabatic transitions. Such mixed quantum/classical studies are at the frontier of current theoretical and computational chemistry [197–204].

From this perspective, it is exciting to perform TRPES of liquids and explore non-adiababtic electronic dynamics in solution, particularly in water. TRPES of liquids has been obstructed for decades by inherent technical difficulties; this long-standing impedance, however, is now gradually being removed by vital challenges of experimentalists. The following three sections are devoted to describe this new frontier of TRPES.

6.1. *Background: photoelectron spectroscopy of liquids*

Photoelectron spectroscopy of liquids, without time resolution, has a history over three decades since the pioneering work of liquid ESCA by Hans Siegbahn, Kai Siegbahn and their coworkers; a compact and excellent review article of liquid ESCA is available by Siegbahn [205]. Introduction of volatile liquids into a high-vacuum chamber is never simple; a number of intriguing ideas, including a moving wire wetted with a sample solution, have been proposed and tested, and have partly succeeded. The great endeavours for introducing liquid samples into a high-vacuum chamber are similar, in some sense, to those in LCMS (liquid chromatography mass spectrometry); the clear difference, however, is that LCMS requires evaporation of solvents to measure the masses of solutes while photoelectron spectroscopy should retain solvation shell at an ambient temperature to study structures and dynamics of liquids. The technical difficulty of sample introduction into the vacuum has impeded wide application of liquid ESCA to chemical problems.

Faubel and coworkers have demonstrated a fast-flowing thin liquid jet as a promising new method for introducing volatile liquids into a high-vacuum chamber [206–209].

Table 1. Comparison of photoionisation threshold, electron binding energy, CTTS band centre in aqueous solutions and electron affinity in gas phase (eV).

	Photoemission threshold[a]	Binding energy[b] $^2P_{3/2}$ and $^2P_{1/2}$	CTTS band	Electron affinity (gas) $^2P_{3/2}$ and $^2P_{1/2}$
Cl^-	8.7	8.7/9.6	7.0	3.6/3.7
Br^-	7.9	8.1/8.8	6.3	3.4/3.8
I^-	7.2	7.7/8.8	5.4	3.1/4.0

Notes: [a]From Watanabe *et al.* [220].
[b]From Winter *et al.* [222].

Although a similar liquid flow technique has already been used in liquid ESCA, Faubel's approach uses a minute diameter (7 μm) high speed (130 m/s) liquid jet. The small diameter minimises the surface area from which evaporation occurs, and the high speed enables quick transport of the sample from a nozzle to a photoionisation point, before extensive evaporative cooling occurs. A thin Pt–Ir metal disc with a μm-aperture was initially used as a discharge nozzle for the liquid [210], but a fused-silica capillary is more convenient for frequent change [211]. The high aspect ratio (channel length/diameter) of a capillary is also more advantageous to a thin disc for generation of a laminar flow [212,213]. Faubel and coworkers have performed UV photoelectron spectroscopy of liquids using an incoherent He(I) discharge lamp; more recently, Faubel, Winter, Hertel and coworkers have performed experiments using the third-generation synchrotron radiation facility (BESSY) [209,214–218], which provides a small beam diameter, wavelength tunability, high photon energies and a high photon flux. A comprehensive and illuminating review of one-photon photoelectron spectroscopy of liquids, prior to TRPES, is available by Winter and Faubel on 2006 *Chemical Review* [209].

Another approach pioneered by Delahay and coworkers in 1969 [219], preceding development of liquid ESCA, is photoelectron emission spectroscopy [220,221]. The method measures photoemission from a liquid surface by collecting electron using an electrode placed close the surface. The photoemission yield is measured as a function of the photon energy, from which the photoemission energy threshold is determined. Photoelectron emission spectroscopy is action spectroscopy, and it does not analyse the kinetic energy distribution of photoelectrons. In fact, if the distribution is observed under typical experimental conditions for this method, the distribution must differ significantly from the original owing to inelastic scattering of electrons with gas species during travelling from the liquid surface to the electrode. Watanabe *et al.* have used a rotating disk wetted with aqueous solutions for photoelectron emission spectroscopy using vacuum UV radiation [220].

Table 1 compares the vertical electron binding energies of halogen anions in aqueous solutions measured by photoelectron spectroscopy [222] with the threshold energy reported by photoelectron emission spectroscopy [220]. Each electron binding energy lists two different values corresponding to the $^2P_{1/2}$ and $^2P_{3/2}$ fine structure levels of the neutral halogen atoms. In principle, the threshold energy corresponds to the red edge of the first photoelectron band, and therefore it should be smaller than the vertical binding energy determined from the centre of the first photoelectron band; the reported threshold energies are in fair agreement with this expectation. For virtually all molecular systems, vertical binding energies are larger than the adiabatic electron binding energies because of the structural deformation upon photoionisation/photodetachment. In solvated systems, removal/creation of a charge significantly destabilises solvation structures and, therefore, the Franck–Condon region is away from the equilibrium structure in the final state: the energy difference between the Franck–Condon region and the potential minimum corresponds to solvent reorganisation energy around the solutes. Consequently, polarisable continuum model of solvents assuming fully relaxed geometries does not reproduce the experimental electron binding energies of an anion and a neutral. This failure is less significant for a cation, because solvents are already ordered around it, and photoionisation does not induce significant change in the solvation structure around a dication. Solvation models such as a reference interaction site model self-consistent field method [223], mixed quantum mechanics/molecular mechanics (QM/MM) calculations or beyond are required for appropriate theoretical modelling of molecular solvation, although agreement with experimental results may still be semi-quantitative. Table 1 also lists the electron affinities of halogen anions in the gas phase; the differences of electron binding energies are greater in solution than in the gas.

The electron binding energies listed in Table 1 were obtained by photoelectron spectroscopy at BESSY using 1–4 M aqueous alkali halide solutions [222]. Similarly high concentrations were also used by photoelectron emission spectroscopy [220]. The need of such high concentration, owing to low sensitivity of the method, is problematic in application to biological systems. Further improvement of the sensitivity is required for soft X-ray photoelectron spectroscopy of liquids. On the other hand, TRPES of liquids has already been performed at the concentration less than 100 mM.

A crucial quantity in photoelectron spectroscopy of condensed matter is the escape depth of an electron. Although excitation light has a large penetration depth into liquids, electrons created far from the liquid surface cannot escape from the liquid owing to inelastic scattering by solvents. The inelastic mean free path (IMFP) of an electron in bulk material depends on the electron kinetic energy; experimental and theoretical studies on IMFP in various solids revealed that IMFP takes the minimum value (typically $\sim$1 nm) at around 50–100 eV and increases in both lower and higher energy sides [26,27,224–227]. This dependence of IMFP plotted against the photoelectron kinetic energy is very similar for all materials and referred to as 'universal curve': this property has been utilised in ESCA to obtain the depth profile of the elements near the solid surface [224]. Figure 27 shows the calculated IMFP in liquid water, as an inversed value, as a function of electron kinetic energy: the inverse IMFP of 100 μm^{-1} corresponds to IMFP of 10 nm [225]. The calculations become increasingly inaccurate in low kinetic energy region ($<$20 eV) owing to the failure of approximations; therefore, the estimated IMFP at low energy is regarded as a guideline. Nonetheless, Figure 27 suggests that TRPES increases its bulk sensitivity and photoemission efficiency at low photoelectron kinetic energy. Accurate treatment of IMFP at low energy requires a Monte-Carlo simulation.

Elastic and inelastic scattering of a photoelectron can occur also in the gas phase above the liquid surface. While the electron scattering in the liquid is inevitable, the scattering in the gas phase can be reduced by experimental conditions. The guidelines for experimental conditions, proposed by Siegbahn [205], to avoid inelastic scattering of electrons after their

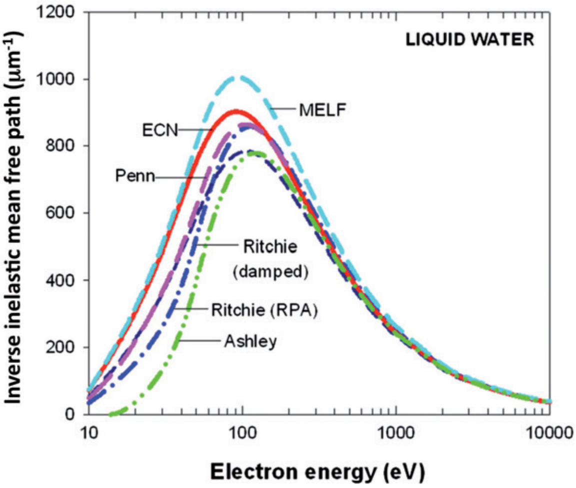

Figure 27. (Colour online) The inverse of an IMFP plotted as a function of electron energy calculated by different extension algorithms to extrapolate the inelastic hard X-ray scattering data. The plot compares different algorithms. The details of these models can be found in the original paper. Adapted with permission from Ref. [225] (Copyright 2012 Informa Plc.).

emission from the liquid surface is $pd \leq 0.1$ Torr mm for the UV region, while $pd \leq 1$ Torr mm for X-ray region, where p is the vapour pressure of solvent and d is the distance between the liquid surface and the entrance slit of an electron spectrometer. The condition is ten times stricter in the UV than in the X-ray region owing to a larger inelastic scattering cross section at lower kinetic energy. Thus, without exception, an electron spectrometer for liquids has an entrance aperture very close to the liquid surface: a typical distance d is several mm. If the saturation vapour pressure p is low, it reduces the experimental difficulty of photoelectron spectroscopy. Morgner and coworkers, therefore, performed He(I) UV photoelectron spectroscopy of highly concentrated aqueous CsF solutions running down a groove in a stainless steel rod: the addition of salt reduced the vapour pressure considerably and enabled their experiment [228]. For wider application of photoelectron spectroscopy to liquids, the experimental method is required to be able to study liquids with high vapour pressure: a liquid beam enables this.

A liquid beam injected into vacuum undergoes evaporative cooling and its temperature diminishes. Therefore, the temperature should be measured at the observation point. The liquid temperature has been determined using the temperature dependence of a Raman band profile [211,229].

6.2. *Liquid TRPES at ultralow kinetic energy*

In 2010, two research groups presented TRPES of liquids at the same time. Siefermann *et al.* [230] performed an experiment using 267 nm pump +32 nm probe pulses and a linear TOF electron energy analyser, whereas Tang *et al.* [231] performed liquid TRPES using 225 nm pump +260 nm probe pulses and a hemispherical energy analyser. The probe

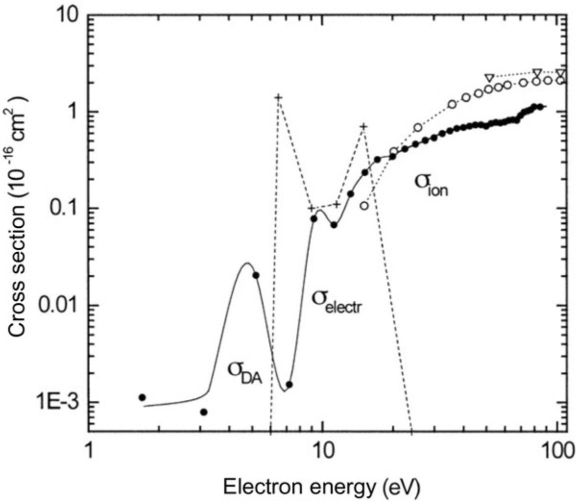

Figure 28. Integral cross section (shown by dots) ascribed to the sum of DA, vibrational excitation above 1 eV energy loss, electronic excitations (electr), as well as ionisation (ion) processes in amorphous ice. Electron scattering cross section reported for electronic excitations of water in the gas phase are indicated with '+'. Measured total electron impact ionisation cross sections for water in the gas phase are shown with ○ and ▽. Adapted with permission from Ref. [271]. (Copyright 2003 Radiation Research Society).

photon energy of the former experiment was sufficiently large to induce photoemission from all chemical species in solution. Consequently, Siefermann *et al.* detected the two-colour signal, which was four orders of magnitude smaller than the one-colour photoelectron signal of solvent water; they ascribed the small signal to a hydrated electron [197,230–269]. As discussed in Section 5.4, the pump–probe experiment using the vacuum UV or extreme UV radiation is challenging, as a high-energy photon can ionise ground-state molecules and decreases the contrast ratio between the two- and one-colour signals (Figure 26). The probe photon energy in the latter experiment was smaller than the electron binding energy of the ground-state molecules, and the two-colour signal was selectively observed. Lubcke *et al.* [269] constructed a magnetic bottle photoelectron spectrometer for liquid TRPES.

The IMFP shown in Figure 27 suggests that the mean free path increases dramatically for electron kinetic energies less than the band (HOMO–LUMO) gap (~7 eV) of bulk water [231,270], because low energy electrons cannot excite bulk water electronically. Tang *et al.* attempted to extend the probing depth of liquid TRPES by restricting the electron kinetic energy to be less than 5 eV. At such low electron kinetic energies, an electron undergoes only vibrational inelastic scattering with or dissociative attachment (DA) to a water molecule. Although no experimental data are available for electron–liquid water scattering, Michaud *et al.* [271] have performed detailed experiments on inelastic scattering of an electron in amorphous ice [271]. Figure 28 shows the measured integral cross sections of the inelastic scattering with the electron energy loss larger than 1 eV. The result clearly indicates that the cross section diminishes by nearly three orders of magnitudes for $E < 8$ eV, as Tang *et al.* [270] have argued. The vibrational inelastic scattering channels are open in this energy range, while the vibrational excitations have the propensity rule of $\Delta v = 1$, so that a single collision rarely induces the energy loss more than 1 eV.

Since the absolute probing depth of photoelectron spectroscopy of water is not accurately known (at any kinetic energy), Tang *et al.* have examined charge-transfer-to-solvent (CTTS) reaction in aqueous NaI solution using TRPES and examined the time constants. These time constants agree well with those reported by transient absorption spectroscopy [270], suggesting that the probing depth of TRPES at kinetic energies lower than 5 eV is sufficiently large to probe properties of bulk solution. Independently, Sager *et al.* [272] have performed time-resolved second harmonic generation (SHG) spectroscopy of water/air interface for 2 M aqueous NaI solution: they photodetached I^-(aq) with a 250 nm pump pulse and observed SHG with a time-delayed 1400 nm probe pulse. The SHG time profile was well explained with the CTTS time constants previously reported for bulk NaI solution. Since no SHG is anticipated for centrosymmetric media within the electric-dipole approximation, SHG is often attributed to the interface where the symmetry is broken. Careful consideration of the SHG mechanism, however, reveals that the electric field gradient near the interface makes anisotropy in the medium and enables SHG even below the interface [273]. To examine this possibility, Sager *et al.* added 1-decanol or hexaethyleneglyocol dodecyl ether and evaluated the change of the SHG signal: they found the former does not alter the SHG signal while the latter decreases the signal by a factor of 2. The essential difference between these two compounds is that the former spreads on the surface as a thin monolayer, while the latter compound extends its polar group into the bulk side for 1–2 nm. Sager *et al.* suggested that the SHG signal largely originates from the region below the Gibbs dividing surface (interface). The result indicates that CTTS dynamics in aqueous NaI solution near the air–liquid interface is similar to those in bulk solution. This seems reasonable in view of the high permittivity of bulk water: quantum chemical calculations have also shown the similarity of the electronic states of I^- near the interface and in isotropic environment in the bulk [274]. Thus, although the absolute probing depth of liquid TRPES is not established yet at this point, its effective probing depth seems sufficiently large to probe structure and dynamics of bulk aqueous solutions. Notice that the surface sensitivity of photoelectron spectroscopy is determined not only by the probing depth, but also by the surface activities of chemical species. When a solute is surface active, the signal arises predominantly from the interface [275].

There is always unavoidable elastic scattering of electrons in bulk water. Tang *et al.* [270] have examined PAD in TRPES of liquid by rotating the polarisation of the laser with respect to the photoelectron detector axis and found no noticeable dependence on polarisation. It is interesting to examine further whether PAD is totally scrambled by elastic scattering of electrons or it carries useful information, as we have seen for TRPES of gases.

There is an unfavourable characteristic of a liquid beam; that is electrokinetic charging [206,212,276,277]. A liquid beam is spontaneously charged because the electrical double layer, created around the inner wall of a fused-silica capillary, is disrupted between the moving phase and the still phase to cause charge separation. The 'streaming potential' thus created can be quite large: a liquid beam of pure water creates a potential of over 10 V [206]. Thus, suppression and/or measurement of the streaming potential are indispensable in photoelectron spectroscopy of liquids. Figure 29 shows the TOF spectra of

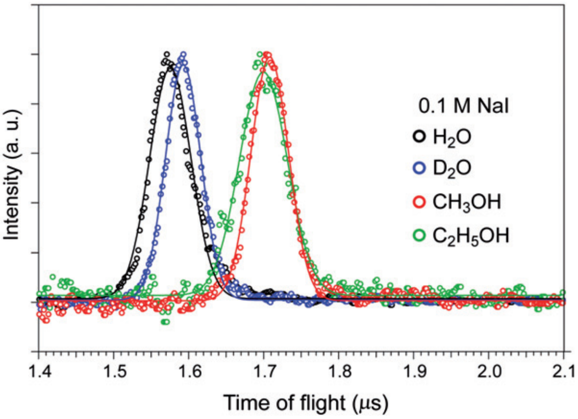

Figure 29. (Colour online) Electron TOF spectra observed for $(1 + 1')$ resonance two-photon ionisation of NO in the presence of liquid beams of 0.1 M NaI solution in H_2O (black), D_2O (blue), methanol (green) and ethanol (red). The solid lines show Gaussian functions obtained by the least squares fit. The widths of TOF signal correspond to the energy width of ca. 60 meV. Adapted with permission from Ref. [278] (Copyright 2012 Elsevier).

photoelectrons produced by $(1 + 1')$ two-photon ionisation of nitric oxide in the vicinity of liquid beams of 0.1 M NaI solution in various solvents [278]. Liquid beams of alcohol solutions are positively charged and their potentials are *ca* 0.1 eV; consequently, photoelectrons ejected from nitric oxide in the vicinity of these liquid beams are decelerated. On the contrary, liquid beams of aqueous solutions are neutral or slightly negatively charged, so that photoelectrons are repelled by the liquid beams and kinetic energies increase.

Finally, an ambient pressure photoelectron spectrometer is a promising new instrument for studies of heterogeneous reactions at the gas–solid and gas–liquid interfaces [279]. TRPES will also be possible with this type of spectrometer.

6.3. *CTTS reaction*

A single water molecule cannot capture an excess electron; bulk water, however, stabilises an electron by orienting OH bonds of the surrounding water molecules towards the centre of the electron cloud [233–236,254–256,258,259,265–267]. The electron binding energy of a hydrated electron in bulk water is *ca* 3.4 eV, as discussed later, with respect to the vacuum level. A hydrated electron is a localised electronic state in the band gap region of a bulk water created by the defect of hydrogen-bonding network (Figure 30). The electron binding energy of a hydrated I^- atom is 7.7 eV, as seen in Table 1; thus, $I^-(aq)$ is also a localised electronic state in the band gap. When $I^-(aq)$ is photoexcited to a metastable excited state below the conduction band, an excess electron cannot be ejected freely into the bulk; the electron cloud can, however, penetrate into the adjacent space between water molecules to be trapped as a hydrated electron. Internal conversion to the ground state of

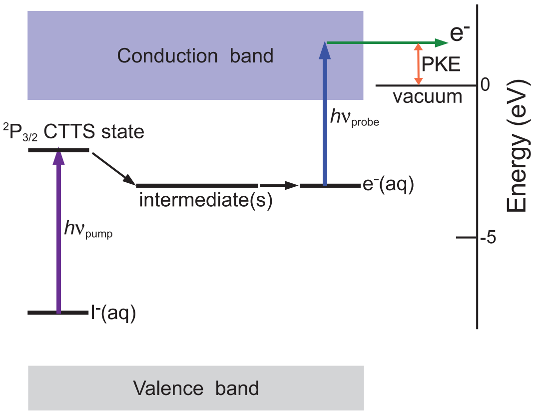

Figure 30. (Colour online) Schematic energy diagram for TRPES of CTTS reaction. Reprinted with permission from Ref. [287] (Copyright 2011 Royal Society of Chemistry).

I^-(aq) competes with this CTTS reaction. When accommodating the excess electron, a local hydrogen-bonding network has to change drastically by reorienting water molecules. Thus, CTTS reaction involves solvation dynamics as the key element. For the studies of CTTS dynamics, I^-(aq) is a suitable solute, as it has no internal degrees of freedom besides electronic motion that would otherwise complicate the problem considerably. CTTS reaction from the lowest ($^2P_{3/2}$) CTTS state of I^- (aq) to water has been previously studied in detail by transient absorption spectroscopy [280–286].

CTTS reaction from I^-(aq) to bulk water is the first system studied by liquid TRPES. I^-(aq) in water is excited by 226 nm pump pulse and subsequent species are photodetached with time-delayed 260 nm probe pulse (Figure 30). Figure 31 shows the photoelectron signal intensity, $I(t)$, observed for aqueous NaI solutions of H_2O and D_2O as a function of delay time. Each point indicates the total photoelectron signal integrated over all kinetic energy distribution at each delay time. The 260 nm pulse induce photoemission from the CTTS state, intermediate, and hydrated electron; therefore, the decay of the photoelectron intensity is attributed to internal conversion to the ground state of I^-(aq), i.e. geminate recombination of an electron and a neutral iodine atom. Figure 31 shows clear isotope effects: the reduction of photoelectron intensity in the first few picoseconds is greater in D_2O than H_2O, while the contrary is true in the next 30 ps. The time constants determined for CTTS in H_2O agreed quite well with those reported by transient absorption spectroscopy.

Figure 32 shows $\sigma(E, t)$, of CTTS reactions in H_2O and D_2O. The horizontal axis has a logarithmic scale to display the rapid spectral change in $\sigma(E, t)$ within 1 ps. The general features of $\sigma(E, t)$ are similar between H_2O and D_2O, however, the spectral width of $\sigma(E, t)$ is narrower and its intensity diminishes faster in D_2O than in H_2O.

The observed photoelectron intensity and spectral evolution can be well explained by either a kinetic model or a diffusion model. Figure 32(c) and (d) shows the time–energy maps of $\sigma(E, t)$ fitted by the kinetic model shown graphically in Figure 33. The initial step from the CTTS state to the first intermediate causes almost only a spectral shift; this step is

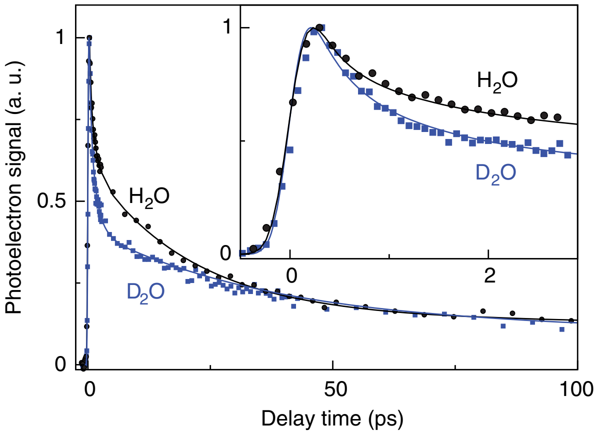

Figure 31. Photoelectron signal intensity as a function of pump–probe time delay observed for CTTS reaction from I^- to bulk water: the sample solutions were 0.1 M aqueous NaI solution in H_2O (black) and D_2O (blue). The schematic energy diagram of the experiment is shown in Figures 5–17. The cross-correlation of the pump and probe laser pulses was ca. 300 fs. A hemispherical electron energy analyser was used to measure a photoelectron spectrum at each time delay, and the spectrum was integrated over photoelectron kinetic energy to obtain the each data point. Adapted with permission from Ref. [287] (Copyright 2011 Royal Society of Chemistry).

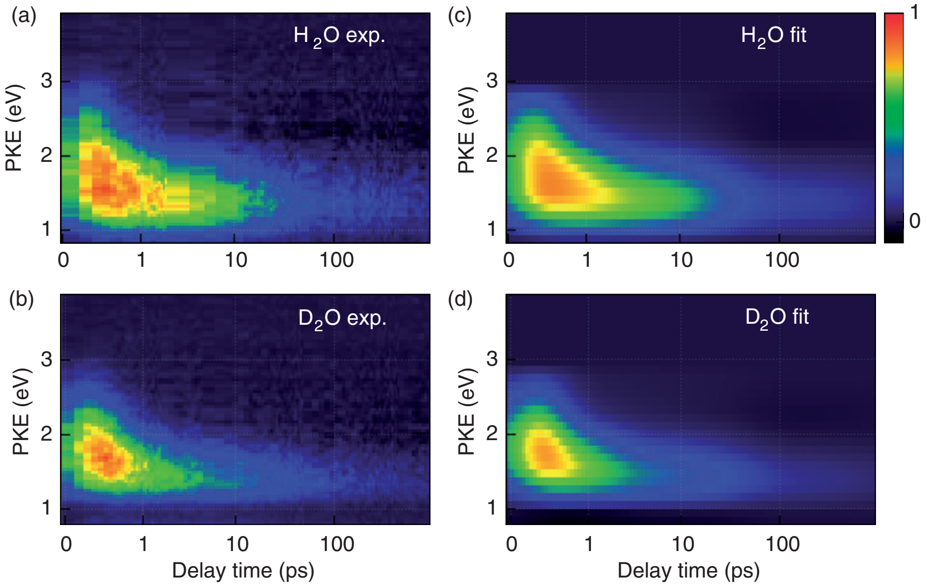

Figure 32. Two-dimensional false colour map for photoelectron kinetic energy distributions measured for CTTS reaction from I^- to bulk water at different pump–probe time delays. The schematic energy diagram of our experiment is shown in Figures 5–17. Panels (a) and (b) are experimental data for 0.1 M aqueous NaI solution in H_2O and D_2O, respectively. Panels (c) and (d) are the results of global fitting of experimental data using a kinetic model. Adapted with permission from Ref. [287] (Copyright 2011 Royal Society of Chemistry).

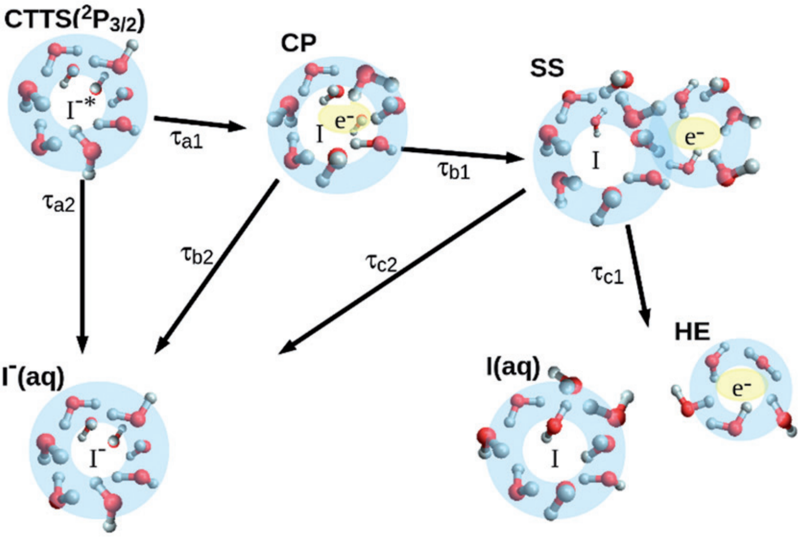

Figure 33. (Colour online) Graphical presentation of our kinetic model with some representative time constants for CTTS reaction from I$^-$ to bulk water. The observed experimental results can be explained comparably well by a kinetic model presented here and a diffusion model. The latter solves a diffusion equation with an assumed interaction potential, e.g. a Morse potential.

expressed by a kinetic equation in both models. The difference between the kinetics and diffusion models lies as to how to express separation of an electron and an iodine atom. The kinetic model assumes two intermediate(s) (possibly a contact pair and a solvent separated state) to reproduce the observed double exponential decay. The diffusion model assumes only one intermediate complex between an electron and an iodine atom, which interact with each other in a Morse potential, and that they mutually diffuse away to produce a free hydrated electron and an iodine atom. The diffusion model assumes that the recombination of an electron and an atom occurs at a certain critical distance set as a boundary condition [283,288]. By adjusting the potential parameters, the diffusion model can express multiple exponential decay behaviour with a single potential. The diffusion model is more appropriate for describing the final separation of the electron and the iodine atom; however, neither of these models can clearly determine how many reaction intermediates are present in the course of this reaction.

A common shortcoming of the analyses of TRPES and transient absorption spectroscopy is that the spectral evolution due to vibrational cooling is neglected by assuming a single spectrum for each transient species. Another issue encountered in the analyses of TRPES and transient absorption spectroscopy is that relative magnitudes of the electronic transition dipole moments may not be accurately known for different chemical species, which potentially causes errors in the estimates of quantum yields. These points should be carefully considered depending on each reaction.

6.4. *Solvated electron*

The CTTS reaction for bulk water discussed in the preceding section ultimately creates hydrated electrons [197,230–259,263–269,289,290]. The hydrated electron is the most important transient species in radiation chemistry and biology; its electron binding energy, however, has not been measured by any means. In 1990s, researchers have found that the electron binding energy of negatively charged molecular clusters varies approximately with $n^{1/3}$ where n is the number of water molecules in the cluster. This trend agrees qualitatively with a model of an electron in a spherical dielectric cavity. In 1990, Coe, Bowen and their coworkers [245] have estimated the electron binding energy of a hydrated electron in bulk water by extrapolating the vertical electron binding energies of negatively charged water clusters to the infinitely large size of the cluster. The value obtained by their analysis was 3.3 eV. Theoretical calculations, however, have refuted this estimate by showing that the electron binding energy varies with $n^{1/3}$ even when the excess electron is trapped at the surfaces of clusters. Since the cluster anions are generated by electron attachment to cold neutral clusters in molecular beams, the energetic penalty is large for an excess electron to penetrate into a cluster by disrupting hydrogen-bonding network; consequently, an electron is trapped at the surface of cold clusters. Neumark and coworkers have discovered that there are three different isomers (I–III) for negatively charged water clusters, in which isomer I exhibits the largest electron binding energy [254,255,289–292]. Careful experiments have revealed that isomer I is created only when the cluster temperature is high, which agrees with the speculation that some structural fluctuation of the neutral cluster is necessary for internalising an excess electron by breaking hydrogen-bonding network in the cluster. Isomers I–III have three different asymptotic values of electron binding energies at the infinitely large sizes of the clusters, in which isomer I is regarded as an embryont of a hydrated electron in the bulk [247], while isomer II seems related to a hypothesised surface state of a hydrated electron [265,291–294].

Tang *et al.* and Siefermann *et al.* have measured the vertical electron binding energy of a hydrated electron in bulk water to be 3.27 and 3.3 eV, respectively. So far, four research groups have reported the electron binding energy of a hydrated electron, which are listed in Table 2. The discrepancy in the experimentally measured VBEs of a hydrated electron indicates experimental errors, which are possibly due to (a) low signal-to-noise ratio, (b) the short IMFP of an electron in liquid, (c) the streaming potential of liquid and (d) inelastic scattering of electrons in the gas phase. As for (a), an excellent signal-to-noise ratio was obtained by magnetic bottle TOF spectroscopy by Lubcke *et al.* [269], while other three experiments have suffered from lower signal-to-noise ratios. As for (b), the experiment by Siefermann *et al.* [230] has a short IMFP because of a high probe photon energy, while other three experiments have bulk sensitivities. As for (c), Tang *et al.* and Siefermann *et al.* have calibrated the observed electron kinetic energy distributions against streaming potentials of liquid beams; the streaming potential varies not only with solutions as shown in Figure 29 but also with conditions of capillaries. As for (d), a magnetic bottle TOF analyser used by Lubcke *et al.* may increases the influence of inelastic collisions, as the magnetic bottle deflects electron trajectories towards a detector in which the electron flying for a longer distance in high molecular density regions may be detected. Finally, Shreve *et al.* [268] used a nanosecond one-colour experiment, while other three TRPES experiments measured the photoelectron spectra of hydrated electrons at the time delays of 100–400 ps. The influence of this difference in time delay is not clear yet.

Table 2. Vertical binding energies (eV) of solvated electrons.

Solvent	Horio *et al.* [278] ⟨E⟩[a]	Horio *et al.* [278] Gauss fit	Tang *et al.* [231]	Shen *et al.* [295]	Siefermann *et al.* [230]	Lubcke *et al.* [269]	Shreve *et al.* [268]
H_2O	3.42(6)	3.44(3)	3.27	–	1.6/3.3[b]	3.4[b]	3.6[b]
D_2O	3.47(5)	3.49(3)	3.20	–	–	–	–
Methanol	3.38(4)	3.36(2)	–	3.1	–	–	–
Ethanol	3.30(3)	3.28(2)	–	3.1	–	–	–

Notes: The numbers within parentheses are 1σ of the last digit.
[a] Expectation values calculated from the observed photoelectron spectra.
[b] Uncorrected for streaming potentials.

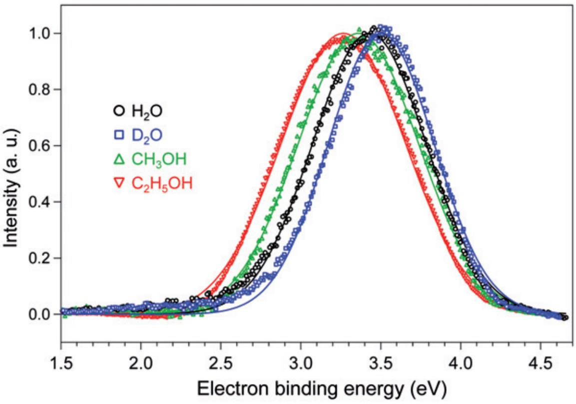

Figure 34. (Colour online) Photoelectron spectra of solvated electrons in bulk solutions: H_2O (black), D_2O (blue), methanol (green) and ethanol (red). Open circles are experimental data and solid lines are the best-fit Gaussian functions obtained by the least squares fitting. The top panel shows residues of the least squares fitting. There was no signal in the energy region of 0–1.5 eV. Adapted with permission from Ref. [278] (Copyright 2012 Elsevier).

In order to achieve higher precision and reliability for liquid TRPES, we have constructed a high-resolution TOF spectrometer coupled with a 100 kHz deep UV femtosecond laser described in Section 4.3. The TOF spectrometer (flight length: 1 m) achieves the energy resolution of 20–60 meV. The repetition rate of 100 kHz is two orders of magnitude higher than those in previous studies, which considerably improves the signal-to-noise ratio. The spectra of solvated electrons in H_2O, D_2O, methanol and ethanol measured at the pump–probe time delay of 2 ns are shown in Figure 34. Striking feature of these spectra is their symmetric Gaussian shapes. It is noted that photoabsorption spectra of solvated electrons in bulk solutions as well as photoelectron spectra of water cluster anions exhibit asymmetric band shapes, which are expressed with Gaussian and Lorentzian. The electron binding energies of solvated electrons thus determined from high-precision measurements are listed in Table 2.

Liquid TRPES has now established a methodology to obtain a spectrum with high precision and efficiency. Application of this methodology to other chemical problems in solution, including dynamics of hydrated electrons and hydrated molecules, are rapidly expanding.

7. Conclusion

TRPES is a highly useful experimental method to study ultrafast electronic deactivation processes and the associated vibrational wave packet dynamics. TRPES of prototypical aromatic molecules requires ultrashort laser pulses in the deep UV region, and its technical difficulty has impeded the studies on ultrafast internal conversion through conical intersection. The multi-colour filamentation technique enables production of deep UV and vacuum UV pulses of less than 20 fs duration; therefore, this technique is highly useful for TRPES at high time-resolution. PAD is sensitive to the electronic character of the ionised state, and time–energy mapping of anisotropy parameter enables clear identification of the change of adiabatic states as presented for the pyrazine case. On the other hand, the case of benzene and toluene suggests that TRPES can also detect the change of the electronic character (electron configuration) along the adiabatic reaction path. In these molecules, the changes of electronic characters are closely tied to molecular structural deformation from planar to non-planar geometry. Furan represents the importance of interplay between experiment and theory in elucidating complex dynamics of polyatomic molecules. For these gas phase reactions, measurements of photoelectron angular anisotropy were the key to elucidating ultrafast electronic dynamics.

Non-adiabatic electronic dynamics in solution is the frontier of experimental and theoretical studies of non-adiabatic dynamics. Inherent technical difficulties associated with TRPES of liquids are now gradually removed, and the research opportunity of liquid TRPES is expanding. The probing depth of liquid TRPES is still not known accurately, and it should be clarified in future study. It is stressed that the great strength of liquid TRPES is that it enables detailed ultrafast photoelectron spectroscopic studies of electron dynamics under wet conditions for electrons, atoms, molecules and particles. The advantage of a high-repetition laser is quite clear for liquid TRPES. TRPES provided the electron binding energies of solvated electrons in four polar protic solvents. These results firmly established energetics of these species. The correspondence of the electron binding energies between cluster anions and the bulk solutions still requires more experimental and theoretical investigations, in which the temperature dependence of electron binding energies should be taken into account. If the PAD is scrambled by elastic scattering, liquid TRPES will rely solely on the one-dimensional information of photoelectorn kinetic energy distribution. Further examination will clarify whether the angular distribution is observable in liquid TRPES. If so, as we have seen for isolated molecules and surfaces, time–energy mapping and angular anisotropy will be of great assistance in elucidating ultrafast electronic dynamics in liquids.

Acknowledgements

The author thanks his present and past group members who made great experimental contribution to TRPES: Y. Suzuki, T. Fuji, Y. Tang, T. Horio, H. Kohguchi, Y. Ogi, S.-Y. Liu, H. Shen, K. Sekiguchi and N. Kurahashi. The author also thanks Professors V. Bonacic-Koutechy and R. Mitiric for collaboration on molecular dynamics on the fly and Professor Elliot Bernstein for valuable comments on this article.

References

[1] M. Eigen, Nobel lecture, 1967.

[2] R. G. W. Norrish, Nobel lecture, 1967.

[3] G. Porter, Nobel lecture, 1967.

[4] A. H. Zewail, Angew. Chem. Int. Ed. **39**, 2587 (2000).

[5] M. Hentschel, R. Kienberger, C. Spielmann, G. A. Reider, N. Milosevic, T. Brabec, P. Corkum, U. Heinzmann, M. Drescher, and F. Krausz, Nature **414**, 509 (2001).

[6] P. Corkum and F. Krausz, Nat. Phys. **3**, 381 (2007).

[7] F. Krausz and M. Ivanov, Rev. Mod. Phys. **81**, 163 (2009).

[8] V. Srajer, T. Y. Teng, T. Ursby, C. Pradervand, Z. Ren, S. Adachi, W. Schildkamp, D. Bourgeois, M. Wulff, and K. Moffat, Science **274**, 1726 (1996).

[9] R. Neutze, R. Wouts, D. van der Spoel, E. Weckert, and J. Hajdu, Nature **406**, 752 (2000).

[10] F. Schotte, M. H. Lim, T. A. Jackson, A. V. Smirnov, J. Soman, J. S. Olson, G. N. Phillips, M. Wulff, and P. A. Anfinrud, Science **300**, 1944 (2003).

[11] H. N. Chapman, A. Barty, M. J. Bogan, S. Boutet, M. Frank, S. P. Hau-Riege, S. Marchesini, B. W. Woods, S. Bajt, H. Benner, R. A. London, E. Plonjes, M. Kuhlmann, R. Treusch, S. Dusterer, T. Tschentscher, J. R. Schneider, E. Spiller, T. Moller, C. Bostedt, M. Hoener, D. A. Shapiro, K. O. Hodgson, D. Van der Spoel, F. Burmeister, M. Bergh, C. Caleman, G. Huldt, M. M. Seibert, F. R. N. C. Maia, R. W. Lee, A. Szoke, N. Timneanu, and J. Hajdu, Nat. Phys. **2**, 839 (2006).

[12] A. Aquila, M. S. Hunter, R. B. Doak, R. A. Kirian, P. Fromme, T. A. White, J. Andreasson, D. Arnlund, S. Bajt, T. R. M. Barends, M. Barthelmess, M. J. Bogan, C. Bostedt, H. Bottin, J. D. Bozek, C. Caleman, N. Coppola, J. Davidsson, D. P. DePonte, V. Elser, S. W. Epp, B. Erk, H. Fleckenstein, L. Foucar, M. Frank, R. Fromme, H. Graafsma, I. Grotjohann, L. Gumprecht, J. Hajdu, C. Y. Hampton, A. Hartmann, R. Hartmann, S. Hauriege, G. Hauser, H. Hirsemann, P. Holl, J. M. Holton, A. Homke, L. Johansson, N. Kimmel, S. Kassemeyer, F. Krasniqi, K. Kuhnel, M. N. Liang, L. Lomb, E. Malmerberg, S. Marchesini, A. V. Martin, F. R. N. C. Maia, M. Messerschmidt, K. Nass, C. Reich, R. Neutze, D. Rolles, B. Rudek, A. Rudenko, I. Schlichting, C. Schmidt, K. E. Schmidt, J. Schulz, M. M. Seibert, R. L. Shoeman, R. Sierra, H. Soltau, D. Starodub, F. Stellato, S. Stern, L. Struder, N. Timneanu, J. Ullrich, X. Y. Wang, G. J. Williams, G. Weidenspointner, U. Weierstall, C. Wunderer, A. Barty, J. C. H. Spence, and H. N. Chapman, Opt. Express **20**, 2706 (2012).

[13] B. J. Siwick, J. R. Dwyer, R. E. Jordan, and R. J. D. Miller, Science **302**, 1382 (2003).

[14] J. R. Dwyer, C. T. Hebeisen, R. Ernstorfer, M. Harb, V. B. Deyirmenjian, R. E. Jordan, and R. J. D. Miller, Philos. Trans. R. Soc. London, Ser. A **364**, 741 (2006).

[15] H. Ihee, V. A. Lobastov, U. M. Gomez, B. M. Goodson, R. Srinivasan, C. Y. Ruan, and A. H. Zewail, Science **291**, 458 (2001).

[16] A. H. Zewail, Annu. Rev. Phys. Chem. **57**, 65 (2006).

[17] P. Baum, D. S. Yang, and A. H. Zewail, Science **318**, 788 (2007).

[18] A. Yurtsever and A. H. Zewail, Science **326**, 708 (2009).

[19] V. Jayaraman, K. R. Rodgers, I. Mukerji, and T. G. Spiro, Science **269**, 1843 (1995).

[20] K. R. Rodgers and T. G. Spiro, Science **265**, 1697 (1994).

[21] C. Kotting and K. Gerwert, Chemphyschem **6**, 881 (2005).

[22] P. Kukura, D. W. McCamant, S. Yoon, D. B. Wandschneider, and R. A. Mathies, Science **310**, 1006 (2005).

[23] M. H. Lim, T. A. Jackson, and P. A. Anfinrud, Nat. Struct. Biol. **4**, 209 (1997).

[24] M. Lim, T. A. Jackson, and P. A. Anfinrud, Science **269**, 962 (1995).

[25] J. H. D. Eland, *Photoelectron Spectroscopy* (Butteworth & Co. Ltd., London, 1974).

[26] S. Hufner, *Photoelectron Spectroscopy: Principles and Applications* (Springer-Verlag, Heidelberg, New York, 2003).

[27] T. L. Barr, *Modern ESCA: the Principles and Practice of X-ray Photoelectron Spectroscopy* (CRC Press Inc., Boca Raton, FL, 1994).

[28] N. J. Turro, V. Ramamurthy, and J. C. Scaiano, *Modern Molecular Photochemistry of Organic Molecules* (University Science Books, Sausalito, 2010).

[29] J. Michl and V. Bonacic-Koutecky, *Electronic Aspects of Organic Photochemistry* (Wiley-Interscience, New York, 1990).

[30] J. L. Knee, in *High Resolution Laser Photoionization and Photoelectron Studies*, edited by I. Powis, T. Baer, and C.-Y. Ng (John Wiley & Sons, New York, 1995), pp. 369–406.

[31] W. Radloff, in *Photoionization and Photodetachment (Part I)*, edited by C.-Y. Ng (World Scientific, Singapore, 1999), pp. 127–181.

[32] T. Suzuki and B. J. Whitaker, Int. Rev. Phys. Chem. **20**, 313 (2001).

[33] D. M. Neumark, Annu. Rev. Phys. Chem. **52**, 255 (2001).

[34] T. Seideman, Annu. Rev. Phys. Chem. **53**, 41 (2002).

[35] A. Stolow, Annu. Rev. Phys. Chem. **54**, 89 (2003).

[36] R. E. Continetti and C. C. Hayden, in *Modern Trends in Chemical Reaction Dynamics: Experiment and Theory (Part I)*, edited by X. Yang and K. Liu (World Scientific, Singapore, 2004), pp. 475–528.

[37] T. Suzuki, in *Modern Trends in Chemical Reaction Dynamics: Theory and Experiment (Part I)*, edited by C.-Y. Ng (World Scientific, Singapore, 2004), pp. 529–577.

[38] T. Suzuki, Annu. Rev. Phys. Chem. **57**, 555 (2006).

[39] I. V. Hertel and W. Radloff, Rep. Prog. Phys. **69**, 1897 (2006).

[40] K. L. Reid, Int. Rev. Phys. Chem. **27**, 607 (2008).

[41] A. Stolow, A. E. Bragg, and D. M. Neumark, Chem. Rev. **104**, 1719 (2004).

[42] C. Nordling, E. Sokolowski, and K. Siegbahn, Phys. Rev. **105**, 1676 (1957).

[43] K. Siegbahn, Nobel lecture, Institute of Physics, University of Uppsala, Sweden, 1981.

[44] D. W. Turner and M. I. Al-joboury, J. Chem. Phys. **37**, 3007 (1962).

[45] D. W. Turner, Philos. Trans. R. Soc. London, Ser. A **268**, 7 (1970).

[46] F. I. Vilesov, A. N. Terenin, and B. L. Kurbatoy, Dokl. Akad. Nauk SSSR **138**, 1329 (1961).

[47] M. I. Al-Joboury and D. W. Turner, J. Chem. Soc. 5141 (1963).

[48] C. B. Harris, N. H. Ge, R. L. Lingle, J. D. McNeill, and C. M. Wong, Annu. Rev. Phys. Chem. **48**, 711 (1997).

[49] H. Petek and S. Ogawa, Prog. Surf. Sci. **56**, 239 (1997).

[50] N. H. Ge, C. M. Wong, and C. B. Harris, Acc. Chem. Res. **33**, 111 (2000).

[51] J. Zhao, B. Li, K. Onda, M. Feng, and H. Petek, Chem. Rev. **106**, 4402 (2006).

[52] P. D. Johnson, Rep. Prog. Phys. **60**, 1217 (1997).

[53] T. J. Gay and F. B. Dunning, Rev. Sci. Instrum. **63**, 1635 (1992).

[54] D. Tillmann, R. Thiel, and E. Kisker, Z. Phys. B: Condens. Matter **77**, 1 (1989).

[55] R. Bertacco, M. Marcon, G. Trezzi, L. Duo, and F. Ciccacci, Rev. Sci. Instrum. **73**, 3867 (2002).

[56] T. Okuda, Y. Takeichi, A. Harasawa, I. Matsuda, T. Kinoshita, and A. Kakizaki, Eur. Phys. J. Special Topics **169**, 181 (2009).

[57] T. Okuda, Y. Takeichi, Y. Maeda, A. Harasawa, I. Matsuda, T. Kinoshita, and A. Kakizaki, Rev. Sci. Instrum. **79**, 123117 (2008).

[58] P. Kruit and F. H. Read, J. Phys. E: Sci. Instrum. **16**, 313 (1983).

[59] Y. I. Suzuki and T. Suzuki, Mol. Phys. **105**, 1675 (2007).

[60] S. C. Althorpe and T. Seideman, J. Chem. Phys. **110**, 147 (1999).

[61] T. Seideman, J. Chem. Phys. **107**, 7859 (1997).

[62] P. R. Keller, J. W. Taylor, T. A. Carlson, and F. A. Grimm, J. Electron Spectrosc. Relat. Phenom. **33**, 333 (1984).

[63] D. Mehaffy, P. R. Keller, J. W. Taylor, T. A. Carlson, and F. A. Grimm, J. Electron Spectrosc. Relat. Phenom. **28**, 239 (1983).

[64] P. R. Keller, D. Mehaffy, J. W. Taylor, F. A. Grimm, and T. A. Carlson, J. Electron Spectrosc. Relat. Phenom. **27**, 223 (1982).

[65] D. Mehaffy, P. R. Keller, J. W. Taylor, T. A. Carlson, M. O. Krause, F. A. Grimm, and J. D. Allen, J. Electron Spectrosc. Relat. Phenom. **26**, 213 (1982).

[66] M. N. Piancastelli, P. R. Keller, J. W. Taylor, F. A. Grimm, and T. A. Carlson, J. Am. Chem. Soc. **105**, 4235 (1983).

[67] Y. I. Suzuki and T. Suzuki, J. Phys. Chem. A **112**, 402 (2008).

[68] M. Tsubouchi, B. J. Whitaker, L. Wang, H. Kohguchi, and T. Suzuki, Phys. Rev. Lett. **86**, 4500 (2001).

[69] M. Tsubouchi, B. J. Whitaker, and T. Suzuki, J. Phys. Chem. A **108**, 6823 (2004).

[70] T. Suzuki, L. Wang, and M. Tsubouchi, J. Phys. Chem. A **108**, 5764 (2004).

[71] P. M. Felker, J. Phys. Chem. **96**, 7844 (1992).

[72] P. M. Felker, L. L. Connell, T. C. Corcoran, and P. W. Joireman, Presented at the Picosecond and Femtosecond Spectroscopy from Laboratory to Real World, Los Angeles, CA, 16–19 July 1990, vol. 1209, p. 53.

[73] J. S. Baskin, P. M. Felker, and A. H. Zewail, J. Chem. Phys. **86**, 2483 (1987).

[74] P. M. Felker and A. H. Zewail, J. Chem. Phys. **86**, 2460 (1987).

[75] L. A. Morgan, C. J. Gillan, J. Tennyson, and X. S. Chen, J. Phys. B: At. Mol. Opt. Phys. **30**, 4087 (1997).

[76] R. R. Lucchese, K. Takatsuka, and V. Mckoy, Phys. Rep. Rev. Sect. Phys. Lett. **131**, 147 (1986).

[77] K. Gokhberg, V. Vysotskiy, L. S. Cederbaum, L. Storchi, F. Tarantelli, and V. Averbukh, J. Chem. Phys. **130**, 064104 (2009).

[78] U. Werner, R. Mitric, and V. Bonacic-Koutecky, J. Chem. Phys. **132**, 174301 (2010).

[79] M. Stener, P. Decleva, D. M. P. Holland, and D. A. Shaw, J. Phys. B: At. Mol. Opt. Phys. **44**, 075203 (2011).

[80] M. Stener and P. Decleva, J. Chem. Phys. **112**, 10871 (2000).

[81] M. Born and R. Oppenheimer, Ann. Phys. **84**, 0457 (1927).

[82] M. L. Hause, Y. H. Yoon, and F. F. Crim, J. Chem. Phys. **125**, 174309 (2006).

[83] F. Bernardi, M. Olivucci, and M. A. Robb, Chem. Soc. Rev. **25**, 321 (1996).

[84] W. Domcke, D. R. Yarkony, and H. Koppel, *Conical Intersections: Theory, Computation and Experiment* (World Scientific Publishing Co. Pte. Ltd., Singapore, 2011).

[85] W. Domcke, D. R. Yarkony, and H. Koppel, *Conical Intersections: Electronic Structure, Dynamics & Spectroscopy* (World Scientific Publishing Co. Pte. Ltd., Singapore, 2004).

[86] D. R. Yarkony, Acc. Chem. Res. **31**, 511 (1998).

[87] D. R. Yarkony, Rev. Mod. Phys. **68**, 985 (1996).

[88] J. von Neumann and E. Wigner, Phys. Z. **30**, 467 (1929).

[89] D. H. Mordaunt, M. N. R. Ashfold, and R. N. Dixon, J. Chem. Phys. **104**, 6460 (1996).

[90] D. H. Mordaunt, R. N. Dixon, and M. N. R. Ashfold, J. Chem. Phys. **104**, 6472 (1996).

[91] R. N. Dixon, Mol. Phys. **88**, 949 (1996).

[92] R. N. Dixon, Acc. Chem. Res. **24**, 16 (1991).

[93] I. Ohmine, J. Chem. Phys. **83**, 2348 (1985).

[94] M. Ben-Nun and T. J. Martinez, Chem. Phys. **259**, 237 (2000).

[95] E. Teller, Isr. J. Chem. **7**, 227 (1969).

[96] L. Salem, C. Leforestier, G. Segal, and R. Wetmore, J. Am. Chem. Soc. **97**, 479 (1975).

[97] L. Salem, J. Am. Chem. Soc. **96**, 3486 (1974).

[98] I. J. Palmer, I. N. Ragazos, F. Bernardi, M. Olivucci, and M. A. Robb, J. Am. Chem. Soc. **115**, 673 (1993).

[99] S. Y. Liu, K. Alnama, J. Matsumoto, K. Nishizawa, H. Kohguchi, Y. P. Lee, and T. Suzuki, J. Phys. Chem. A **115**, 2953 (2011).

[100] A. T. J. B. Eppink and D. H. Parker, Rev. Sci. Instrum. **68**, 3477 (1997).
[101] J. J. Lin, J. G. Zhou, W. C. Shiu, and K. P. Liu, Rev. Sci. Instrum. **74**, 2495 (2003).
[102] T. Horio and T. Suzuki, Rev. Sci. Instrum. **80**, 013706 (2009).
[103] Y. Ogi, H. Kohguchi, D. Niu, K. Ohshimo, and T. Suzuki, J. Phys. Chem. A **113**, 14536 (2009).
[104] Y. Tang, Y. I. Suzuki, T. Horio, and T. Suzuki, Phys. Rev. Lett. **104**, 073002 (2010).
[105] G. A. Garcia, L. Nahon, and I. Powis, Rev. Sci. Instrum. **75**, 4989 (2004).
[106] D. M. Niu, Y. Ogi, Y. I. Suzuki, and T. Suzuki, J. Phys. Chem. A **115**, 2096 (2011).
[107] T. Fuji, T. Horio, and T. Suzuki, Opt. Lett. **32**, 2481 (2007).
[108] P. Baum, S. Lochbrunner, and E. Riedle, Opt. Lett. **29**, 1686 (2004).
[109] L. Misoguti, I. P. Christov, S. Backus, M. M. Murnane, and H. C. Kapteyn, Phys. Rev. A: At. Mol. Opt. Phys. **72**, 063803 (2005).
[110] L. Misoguti, S. Backus, C. G. Durfee, R. Bartels, M. M. Murnane, and H. C. Kapteyn, Phys. Rev. Lett. **87**, 013601 (2001).
[111] S. L. Chin, *Femtosecond Laser Filamentation* (Springer, New York, 2010).
[112] E. T. J. Nibbering, G. Grillon, M. A. Franco, B. S. Prade, and A. Mysyrowicz, J. Opt. Soc. Am. B: Opt. Phys. **14**, 650 (1997).
[113] T. Fuji, T. Suzuki, E. E. Serebryannikov, and A. Zheltikov, Phys. Rev. A: At. Mol. Opt. Phys. **80**, 063822 (2009).
[114] Y. I. Suzuki, T. Fuji, T. Horio, and T. Suzuki, J. Chem. Phys. **132**, 174302 (2010).
[115] L. Wang, H. Kohguchi, and T. Suzuki, Faraday Discussions **113**, 37 (1999).
[116] T. Suzuki, L. Wang, and H. Kohguchi, J. Chem. Phys. **111**, 4859 (1999).
[117] M. Oku, Y. Hou, X. Xing, B. Reed, H. Xu, C. Chang, C.-Y. Ng, K. Nishizawa, K. Ohshimo, and T. Suzuki, J. Phys. Chem. A **112**, 2293 (2008).
[118] T. Suzuki, J. Chin. Chem. Soc. **53**, 113 (2006).
[119] M. Tsubouchi, C. A. de Lange, and T. Suzuki, J. Electron Spectrosc. Relat. Phenom. **142**, 193 (2005).
[120] M. Tsubouchi and T. Suzuki, J. Chem. Phys. **121**, 8846 (2004).
[121] M. Tsubouchi and T. Suzuki, J. Phys. Chem. A **107**, 10897 (2003).
[122] Y. Matsumoto, S. K. Kim, and T. Suzuki, J. Chem. Phys. **119**, 300 (2003).
[123] H. Shen, S. Adachi, T. Horio, and T. Suzuki, Opt. Express **19**, 22637 (2011).
[124] J. Piel, E. Riedle, L. Gundlach, R. Ernstorfer, and R. Eichberger, Opt. Lett. **31**, 1289 (2006).
[125] C. Schriever, S. Lochbrunner, P. Krok, and E. Riedle, Opt. Lett. **33**, 192 (2008).
[126] T. Wilhelm, J. Piel, and E. Riedle, Opt. Lett. **22**, 1494 (1997).
[127] A. Shirakawa, I. Sakane, M. Takasaka, and T. Kobayashi, Appl. Phys. Lett. **74**, 2268 (1999).
[128] A. Shirakawa, I. Sakane, and T. Kobayashi, Opt. Lett. **23**, 1292 (1998).
[129] E. Riedle, M. Beutter, S. Lochbrunner, J. Piel, S. Schenkl, S. Sporlein, and W. Zinth, Appl. Phys. B **71**, 457 (2000).
[130] R. Schneider and W. Domcke, Chem. Phys. Lett. **150**, 235 (1988).
[131] L. Seidner, G. Stock, A. L. Sobolewski, and W. Domcke, J. Chem. Phys. **96**, 5298 (1992).
[132] C. Woywod, W. Domcke, A. L. Sobolewski, and H. J. Werner, J. Chem. Phys. **100**, 1400 (1994).
[133] T. Gerdts and U. Manthe, Chem. Phys. Lett. **295**, 167 (1998).
[134] A. Raab, G. A. Worth, H. D. Meyer, and L. S. Cederbaum, J. Chem. Phys. **110**, 936 (1999).
[135] M. Thoss, W. H. Miller, and G. Stock, J. Chem. Phys. **112**, 10282 (2000).
[136] C. Coletti and G. D. Billing, Chem. Phys. Lett. **368**, 289 (2003).
[137] D. V. Shalashilin and M. S. Child, J. Chem. Phys. **121**, 3563 (2004).
[138] X. Chen and V. S. Batista, J. Chem. Phys. **125**, 124313 (2006).
[139] P. Puzari, B. Sarkar, and S. Adhikari, J. Chem. Phys. **125**, 194316 (2006).
[140] P. Puzari, R. S. Swathi, B. Sarkar, and S. Adhikari, J. Chem. Phys. **123**, 134317 (2005).
[141] R. X. He, C. Y. Zhu, C. H. Chin, and S. H. Lin, Chem. Phys. Lett. **476**, 19 (2009).
[142] U. Werner, R. Mitric, T. Suzuki, and V. Bonacic-Koutecky, Chem. Phys. **349**, 319 (2008).

[143] U. Werner, R. Mitric, and V. Bonacic-Koutecky, J. Chem. Phys. **132**, 174301 (2010).
[144] C. K. Lin, Y. L. Niu, C. Y. Zhu, Z. G. Shuai, and S. H. Lin, Chem. Asian J. **6**, 2977 (2011).
[145] E. J. Heller, J. Chem. Phys. **68**, 3891 (1978).
[146] E. J. Heller, Acc. Chem. Res. **14**, 368 (1981).
[147] M. Seel and W. Domcke, J. Chem. Phys. **95**, 7806 (1991).
[148] S. Hahn and G. Stock, Phys. Chem. Chem. Phys. **3**, 2331 (2001).
[149] V. Stert, P. Farmanara, and W. Radloff, J. Chem. Phys. **112**, 4460 (2000).
[150] Y. I. Suzuki, T. Fuji, T. Horio, and T. Suzuki, J. Chem. Phys. **132**, 174302 (2010).
[151] Y. Udagawa, M. Ito, and I. Suzuka, Chem. Phys. **46**, 237 (1980).
[152] K. K. Innes, I. G. Ross, and W. R. Moomaw, J. Mol. Spectrosc. **132**, 492 (1988).
[153] J. C. Tully, J. Chem. Phys. **93**, 1061 (1990).
[154] K. Gokhberg, V. Vysotskiy, L. S. Cederbaum, L. Storchi, F. Tarantelli, and V. Averbukh, J. Chem. Phys. **130**, 064104 (2009).
[155] T. A. Stephenson, P. L. Radloff, and S. A. Rice, J. Chem. Phys. **81**, 1060 (1984).
[156] T. A. Stephenson and S. A. Rice, J. Chem. Phys. **81**, 1073 (1984).
[157] M. Meisl and R. Janoschek, J. Chem. Soc. Chem. Commun. **1986**, 1066 (1986).
[158] A. Toniolo, A. L. Thompson, and T. J. Martinez, Chem. Phys. **304**, 133 (2004).
[159] W. Radloff, T. Freudenberg, H. H. Ritze, V. Stert, F. Noack, and I. V. Hertel, Chem. Phys. Lett. **261**, 301 (1996).
[160] W. Radloff, V. Stert, T. Freudenberg, I. V. Hertel, C. Jouvet, C. Dedonder-Lardeux, and D. Solgadi, Chem. Phys. Lett. **281**, 20 (1997).
[161] P. Farmanara, V. Stert, W. Radloff, and I. V. Hertel, J. Phys. Chem. A **105**, 5613 (2001).
[162] S. H. Lee, K. C. Tang, I. C. Chen, M. Schmitt, J. P. Shaffer, T. Schultz, J. G. Underwood, M. Z. Zgierski, and A. Stolow, J. Phys. Chem. A **106**, 8979 (2002).
[163] Y. Z. Liu, B. F. Tang, H. Shen, S. Zhang, and B. Zhang, Opt. Express **18**, 5791 (2010).
[164] Y. I. Suzuki, T. Horio, T. Fuji, and T. Suzuki, J. Chem. Phys. **134**, 184313 (2011).
[165] T. Fuji, Y. I. Suzuki, T. Horio, T. Suzuki, R. Mitric, U. Werner, and V. Bonacic-Koutecky, J. Chem. Phys. **133**, 234303 (2010).
[166] M. H. Palmer, I. C. Walker, C. C. Ballard, and M. F. Guest, Chem. Phys. **192**, 111 (1995).
[167] A. B. Trofimov and J. Schirmer, Chem. Phys. **224**, 175 (1997).
[168] O. Christiansen and P. Jorgensen, J. Am. Chem. Soc. **120**, 3423 (1998).
[169] J. Wan, J. Meller, M. Hada, M. Ehara, and H. Nakatsuji, J. Chem. Phys. **113**, 7853 (2000).
[170] R. Burcl, R. D. Amos, and N. C. Handy, Chem. Phys. Lett. **355**, 8 (2002).
[171] E. V. Gromov, A. B. Trofimov, N. M. Vitkovskaya, J. Schirmer, and H. Koppel, J. Chem. Phys. **119**, 737 (2003).
[172] E. V. Gromov, A. B. Trofimov, N. M. Vitkovskaya, H. Koppel, J. Schirmer, H. D. Meyer, and L. S. Cederbaum, J. Chem. Phys. **121**, 4585 (2004).
[173] N. Gavrilov, S. Salzmann, and C. M. Marian, Chem. Phys. **349**, 269 (2008).
[174] J. L. Roebber, D. P. Gerrity, R. Hemley, and V. Vaida, Chem. Phys. Lett. **75**, 104 (1980).
[175] E. V. Gromov, C. Leveque, F. Gatti, I. Burghardt, and H. Koppel, J. Chem. Phys. **135**, 164305 (2011).
[176] C. E. Crespo-Hernandez, B. Cohen, P. M. Hare, and B. Kohler, Chem. Rev. **104**, 1977 (2004).
[177] S. Perun, A. L. Sobolewski, and W. Domcke, J. Am. Chem. Soc. **127**, 6257 (2005).
[178] C. T. Middleton, K. de La Harpe, C. Su, Y. K. Law, C. E. Crespo-Hernandez, and B. Kohler, Annu. Rev. Phys. Chem. **60**, 217 (2009).
[179] H. Kang, K. T. Lee, B. Jung, Y. J. Ko, and S. K. Kim, J. Am. Chem. Soc. **124**, 12958 (2002).
[180] C. Canuel, M. Mons, F. Piuzzi, B. Tardivel, I. Dimicoli, and M. Elhanine, J. Chem. Phys. **122**, 074316 (2005).
[181] S. Ullrich, T. Schultz, M. Z. Zgierski, and A. Stolow, Phys. Chem. Chem. Phys. **6**, 2796 (2004).
[182] H. R. Hudock, B. G. Levine, A. L. Thompson, H. Satzger, D. Townsend, N. Gador, S. Ullrich, A. Stolow, and T. J. Martinez, J. Phys. Chem. A **111**, 8500 (2007).

[183] T. Pfeifer, C. Spielmann, and G. Gerber, Rep. Prog. Phys. **69**, 443 (2006).
[184] M. Nisoli and G. Sansone, Prog. Quantum Electron. **33**, 17 (2009).
[185] V. Ayvazyan, N. Baboi, J. Bahr, V. Balandin, B. Beutner, A. Brandt, I. Bohnet, A. Bolzmann, R. Brinkmann, O. I. Brovko, J. P. Carneiro, S. Casalbuoni, M. Castellano, P. Castro, L. Catani, E. Chiadroni, S. Choroba, A. Cianchi, H. Delsim-Hashemi, G. Di Pirro, M. Dohlus, S. Dusterer, H. T. Edwards, B. Faatz, A. A. Fateev, J. Feldhaus, K. Flottmann, J. Frisch, L. Frohlich, T. Garvey, U. Gensch, N. Golubeva, H. J. Grabosch, B. Grigoryan, O. Grimm, U. Hahn, J. H. Han, M. V. Hartrott, K. Honkavaara, M. Huning, R. Ischebeck, E. Jaeschke, M. Jablonka, R. Kammering, V. Katalev, B. Keitel, S. Khodyachykh, Y. Kim, V. Kocharyan, M. Korfer, M. Kollewe, D. Kostin, D. Kramer, M. Krassilnikov, G. Kube, L. Lilje, T. Limberg, D. Lipka, F. Lohl, M. Luong, C. Magne, J. Menzel, P. Michelato, V. Miltchev, M. Minty, W. D. Moller, L. Monaco, W. Muller, M. Nagl, O. Napoly, P. Nicolosi, D. Nolle, T. Nunez, A. Oppelt, C. Pagani, R. Paparella, B. Petersen, B. Petrosyan, J. Pfluger, P. Piot, E. Plonjes, L. Poletto, D. Proch, D. Pugachov, K. Rehlich, D. Richter, S. Riemann, M. Ross, J. Rossbach, M. Sachwitz, E. L. Saldin, W. Sandner, H. Schlarb, B. Schmidt, M. Schmitz, P. Schmuser, J. R. Schneider, E. A. Schneidmiller, H. J. Schreiber, S. Schreiber, A. V. Shabunov, D. Sertore, S. Setzer, S. Simrock, E. Sombrowski, L. Staykov, B. Steffen, F. Stephan, F. Stulle, K. P. Sytchev, H. Thom, K. Tiedtke, M. Tischer, R. Treusch, D. Trines, I. Tsakov, A. Vardanyan, R. Wanzenberg, T. Weiland, H. Weise, M. Wendt, I. Will, A. Winter, K. Wittenburg, M. V. Yurkov, I. Zagorodnov, P. Zambolin, and K. Zapfe, Eur. Phys. J. D **37**, 297 (2006).
[186] T. Shintake, H. Tanaka, T. Hara, T. Tanaka, K. Togawa, M. Yabashi, Y. Otake, Y. Asano, T. Bizen, T. Fukui, S. Goto, A. Higashiya, T. Hirono, N. Hosoda, T. Inagaki, S. Inoue, M. Ishii, Y. Kim, H. Kimura, M. Kitamura, T. Kobayashi, H. Maesaka, T. Masuda, S. Matsui, T. Matsushita, X. Marechal, M. Nagasono, H. Ohashi, T. Ohata, T. Ohshima, K. Onoe, K. Shirasawa, T. Takagi, S. Takahashi, M. Takeuchi, K. Tamasaku, R. Tanaka, Y. Tanaka, T. Tanikawa, T. Togashi, S. Wu, A. Yamashita, K. Yanagida, C. Zhang, H. Kitamura, and T. Ishikawa, Nat. Photonics **2**, 555 (2008).
[187] A. Barty, R. Soufli, T. McCarville, S. L. Baker, M. J. Pivovaroff, P. Stefan, and R. Bionta, Opt. Express **17**, 15508 (2009).
[188] P. Zuo, T. Fuji, T. Horio, S. Adachi, and T. Suzuki, Appl. Phys. B, in press (2012).
[189] M. Ghotbi, M. Beutler, and F. Noack, Opt. Lett. **35**, 3492 (2010).
[190] M. Beutler, M. Ghotbi, F. Noack, and I. V. Hertel, Opt. Lett. **35**, 1491 (2010).
[191] M. Beutler, M. Ghotbi, and F. Noack, Opt. Lett. **36**, 3726 (2011).
[192] S. Y. Liu, Y. Ogi, T. Fuji, K. Nishizawa, T. Horio, T. Mizuno, H. Kohguchi, M. Nagasono, T. Togashi, K. Tono, M. Yabashi, Y. Senba, H. Ohashi, H. Kimura, T. Ishikawa, and T. Suzuki, Phys. Rev. A: At. Mol. Opt. Phys. **81**, 031403 (2010).
[193] S. Y. Liu, Y. Ogi, T. Fuji, K. Nishizawa, T. Horio, T. Mizuno, H. Kohguchi, M. Nagasono, T. Togashi, K. Tono, M. Yabashi, Y. Senba, H. Ohashi, H. Kimura, T. Ishikawa, and T. Suzuki, Phys. Rev. A: At. Mol. Opt. Phys. **81**, 031403 (2010).
[194] Y. Ogi and T. Suzuki, unpublished.
[195] A. Nitzan, *Chemical Dynamics in Condensed Phases: Relaxation, Transfer, and Reactions in Condensed Molecular Systems* (Oxford University Press, Oxford, 2006).
[196] Philos, Trans. R. Soc. London, Ser. B **359**, 1141 (2004).
[197] P. J. Rossky and J. Schnitker, J. Phys. Chem. **92**, 4277 (1988).
[198] M. Tuckerman, K. Laasonen, M. Sprik, and M. Parrinello, J. Chem. Phys. **103**, 150 (1995).
[199] D. Marx, Chemphyschem **7**, 1848 (2006).
[200] A. Toniolo, S. Olsen, L. Manohar, and T. J. Martinez, Faraday Discuss. **127**, 149 (2004).
[201] M. Wohlgemuth, V. Bonacic-Koutecky, and R. Mitric, J. Chem. Phys. **135**, 054105 (2011).
[202] Q. Cui, M. Elstner, E. Kaxiras, T. Frauenheim, and M. Karplus, J. Phys. Chem. B **105**, 569 (2001).

[203] H. Lin and D. G. Truhlar, Theor. Chem. Acc. **117**, 185 (2007).

[204] H. M. Senn and W. Thiel, Angew. Chem. Int. Ed. **48**, 1198 (2009).

[205] H. Siegbahn, J. Phys. Chem. **89**, 897 (1985).

[206] M. Faubel, B. Steiner, and J. P. Toennies, J. Chem. Phys. **106**, 9013 (1997).

[207] M. Faubel, S. Schlemmer, and J. P. Toennies, Z. Physik D **10**, 269 (1988).

[208] M. Faubel, in *Photoionization and Photodetachment*, edited by C.-Y. Ng (World Scientific, Singapore, 2000), pp. 634–690.

[209] B. Winter and M. Faubel, Chem. Rev. **106**, 1176 (2006).

[210] M. Faubel and B. Steiner, Ber. Bunsen-Gesellschaft Phys. Chem. Chem. Phys. **96**, 1167 (1992).

[211] K. R. Wilson, B. S. Rude, J. Smith, C. Cappa, D. T. Co, R. D. Schaller, M. Larsson, T. Catalano, and R. J. Saykally, Rev. Sci. Instrum. **75**, 725 (2004).

[212] W. L. Holstein, L. J. Hayes, E. M. C. Robinson, G. S. Laurence, and M. A. Buntine, J. Phys. Chem. B **103**, 3035 (1999).

[213] B. Abedian and A. A. Sonin, J. Fluid Mech. **120**, 199 (1982).

[214] E. F. Aziz, N. Ottosson, M. Faubel, I. V. Hertel, and B. Winter, Nature **455**, 89 (2008).

[215] P. Jungwirth and B. Winter, Annu. Rev. Phys. Chem. **59**, 343 (2008).

[216] B. Winter, U. Hergenhahn, M. Faubel, O. Bjorneholm, and I. V. Hertel, J. Chem. Phys. **127**, 094501 (2007).

[217] R. Weber, B. Winter, P. M. Schmidt, W. Widdra, I. V. Hertel, M. Dittmar, and M. Faubel, J. Phys. Chem. B **108**, 4729 (2004).

[218] B. Winter, R. Weber, W. Widdra, M. Dittmar, M. Faubel, and I. V. Hertel, J. Phys. Chem. A **108**, 2625 (2004).

[219] B. Baron, P. Chartier, P. Delahay, and R. Lugo, J. Chem. Phys. **51**, 2562 (1969).

[220] I. Watanabe, J. B. Flanagan, and P. Delahay, J. Chem. Phys. **73**, 2057 (1980).

[221] P. Delahay, Acc. Chem. Res. **15**, 40 (1982).

[222] B. Winter, R. Weber, I. V. Hertel, M. Faubel, P. Jungwirth, E. C. Brown, and S. E. Bradforth, J. Am. Chem. Soc. **127**, 7203 (2005).

[223] H. Sato, F. Hirata, and S. Kato, J. Chem. Phys. **105**, 1546 (1996).

[224] M. P. Seah and W. A. Dench, Surf. Interface Anal. **1**, 2 (1979).

[225] D. Emfietzoglou, I. Kyriakou, I. Abril, R. Garcia-Molina, and H. Nikjoo, Int. J. Radiat. Biol. **88**, 22 (2012).

[226] D. Emfietzoglou, I. Kyriakou, I. Abril, R. Garcia-Molina, I. D. Petsalakis, H. Nikjoo, and A. Pathak, Nucl. Instrum. Methods Phys. Res., Sect. B **267**, 45 (2009).

[227] N. Ottosson, M. Faubel, S. E. Bradforth, P. Jungwirth, and B. Winter, J. Electron Spectrosc. Relat. Phenom. **177**, 60 (2010).

[228] R. Bohm, H. Morgner, J. Oberbrodhage, and M. Wulf, Surf. Sci. **317**, 407 (1994).

[229] J. D. Smith, C. D. Cappa, W. S. Drisdell, R. C. Cohen, and R. J. Saykally, J. Am. Chem. Soc. **128**, 12892 (2006).

[230] K. R. Siefermann, Y. X. Liu, E. Lugovoy, O. Link, M. Faubel, U. Buck, B. Winter, and B. Abel, Nat. Chem. **2**, 274 (2010).

[231] Y. Tang, H. Shen, K. Sekiguchi, N. Kurahashi, T. Mizuno, Y. I. Suzuki, and T. Suzuki, Phys. Chem. Chem. Phys. **12**, 3653 (2010).

[232] E. J. Hart and J. W. Boag, J. Am. Chem. Soc. **84**, 4090 (1962).

[233] M. Natori, J. Phys. Soc. Jpn. **27**, 1309 (1969).

[234] M. Natori, J. Phys. Soc. Jpn. **24**, 913 (1968).

[235] M. Natori and T. Watanabe, J. Phys. Soc. Jpn **21**, 1573 (1966).

[236] S. Schlick, P. A. Narayana, and L. Kevan, J. Chem. Phys. **64**, 3153 (1976).

[237] F. J. Webster, J. Schnitker, M. S. Friedrichs, R. A. Friesner, and P. J. Rossky, Phys. Rev. Lett. **66**, 3172 (1991).

[238] J. Schnitker, K. Motakabbir, P. J. Rossky, and R. Friesner, Phys. Rev. Lett. **60**, 456 (1988).

[239] J. Schnitker and P. J. Rossky, J. Chem. Phys. **86**, 3471 (1987).

[240] Y. Kimura, J. C. Alfano, P. K. Walhout, and P. F. Barbara, J. Phys. Chem. **98**, 3450 (1994).

[241] J. C. Alfano, P. K. Walhout, Y. Kimura, and P. F. Barbara, J. Chem. Phys. **98**, 5996 (1993).

[242] A. Kammrath, J. R. R. Verlet, G. B. Griffin, and D. M. Neumark, J. Chem. Phys. **125**, 076101 (2006).

[243] A. E. Bragg, J. R. R. Verlet, A. Kammrath, O. Cheshnovsky, and D. M. Neumark, J. Am. Chem. Soc. **127**, 15283 (2005).

[244] A. E. Bragg, J. R. R. Verlet, A. Kammrath, O. Cheshnovsky, and D. M. Neumark, Science **306**, 669 (2004).

[245] J. V. Coe, G. H. Lee, J. G. Eaton, S. T. Arnold, H. W. Sarkas, K. H. Bowen, C. Ludewigt, H. Haberland, and D. R. Worsnop, J. Chem. Phys. **92**, 3980 (1990).

[246] J. V. Coe, A. D. Earhart, M. H. Cohen, G. J. Hoffman, H. W. Sarkas, and K. H. Bowen, J. Chem. Phys. **107**, 6023 (1997).

[247] J. V. Coe, S. M. Williams, and K. H. Bowen, Int. Rev. Phys. Chem. **27**, 27 (2008).

[248] M. J. Tauber and R. A. Mathies, J. Am. Chem. Soc. **125**, 1394 (2003).

[249] M. J. Tauber and R. A. Mathies, Chem. Phys. Lett. **354**, 518 (2002).

[250] M. J. Tauber and R. A. Mathies, J. Phys. Chem. A **105**, 10952 (2001).

[251] M. Mizuno and T. Tahara, J. Phys. Chem. A **105**, 8823 (2001).

[252] M. Mizuno and T. Tahara, J. Phys. Chem. A **107**, 2411 (2003).

[253] M. Mizuno, S. Yamaguchi, and T. Tahara, J. Phys. Chem. A **109**, 5257 (2005).

[254] L. Turi, W. S. Sheu, and P. J. Rossky, Science **310**, 1769 (2005).

[255] L. Turi, W. S. Sheu, and P. J. Rossky, Science **309**, 914 (2005).

[256] L. Turi and A. Madarasz, Science **331**, 1387 (2011).

[257] J. R. Roscioli, N. I. Hammer, and M. A. Johnson, J. Phys. Chem. A **110**, 7517 (2006).

[258] I. A. Shkrob, J. Phys. Chem. A **111**, 5223 (2007).

[259] I. A. Shkrob, W. J. Glover, R. E. Larsen, and B. J. Schwartz, J. Phys. Chem. A **111**, 5232 (2007).

[260] O. Marsalek, F. Uhlig, J. Vandevondele, and P. Jungwirth, Acc. Chem. Res. **45**, 23 (2012).

[261] O. Marsalek, F. Uhlig, and P. Jungwirth, J. Phys. Chem. C **114**, 20489 (2010).

[262] O. Marsalek, F. Uhlig, T. Frigato, B. Schmidt, and P. Jungwirth, Phys. Rev. Lett. **105**, 043002 (2010).

[263] R. E. Larsen, W. J. Glover, and B. J. Schwartz, Science **331**, 1387 (2011).

[264] R. E. Larsen, W. J. Glover, and B. J. Schwartz, Science **329**, 65 (2010).

[265] L. D. Jacobson and J. M. Herbert, J. Am. Chem. Soc. **133**, 19889 (2011).

[266] L. D. Jacobson and J. M. Herbert, Science **331**, 1387 (2011).

[267] J. M. Herbert and L. D. Jacobson, Int. Rev. Phys. Chem. **30**, 1 (2011).

[268] A. T. Shreve, T. A. Yen, and D. M. Neumark, Chem. Phys. Lett. **493**, 216 (2010).

[269] A. Lubcke, F. Buchner, N. Heine, I. V. Hertel, and T. Schultz, Phys. Chem. Chem. Phys. **12**, 14629 (2010).

[270] Y. Tang, Y. I. Suzuki, H. Shen, K. Sekiguchi, N. Kurahashi, K. Nishizawa, P. Zuo, and T. Suzuki, Chem. Phys. Lett. **494**, 111 (2010).

[271] M. Michaud, A. Wen, and L. Sanche, Radiat. Res. **159**, 3 (2003).

[272] D. M. Sagar, C. D. Bain, and J. R. R. Verlet, J. Am. Chem. Soc. **132**, 6917 (2010).

[273] T. F. Heinz, in *Nonlinear Surface Electromagnetic Phenomena*, edited by H.-E. Ponath and G. I. Stegeman (Elsevier, Amsterdam, 1991), pp. 353–416.

[274] S. E. Bradforth and P. Jungwirth, J. Phys. Chem. A **106**, 1286 (2002).

[275] F. Buchner, T. Schultz, and A. Lubcke, Phys. Chem. Chem. Phys. **14**, 5837 (2012).

[276] A. M. Duffin and R. J. Saykally, J. Phys. Chem. C **112**, 17018 (2008).

[277] A. M. Duffin and R. J. Saykally, J. Phys. Chem. C **111**, 12031 (2007).

[278] T. Horio, H. Shen, S. Adachi, and T. Suzuki, Chem. Phys. Lett. **535**, 12 (2012).

[279] M. Salmeron and R. Schlogl, Surf. Sci. Rep. **63**, 169 (2008).

[280] J. A. Kloepfer, V. H. Vilchiz, V. A. Lenchenkov, and S. E. Bradforth, Chem. Phys. Lett. **298**, 120 (1998).

[281] J. A. Kloepfer, V. H. Vilchiz, V. A. Lenchenkov, A. C. Germaine, and S. E. Bradforth, J. Chem. Phys. **113**, 6288 (2000).

[282] V. H. Vilchiz, J. A. Kloepfer, A. C. Germaine, V. A. Lenchenkov, and S. E. Bradforth, J. Phys. Chem. A **105**, 1711 (2001).

[283] J. A. Kloepfer, V. H. Vilchiz, V. A. Lenchenkov, X. Y. Chen, and S. E. Bradforth, J. Chem. Phys. **117**, 766 (2002).

[284] V. H. Vilchiz, X. Y. Chen, J. A. Kloepfer, and S. E. Bradforth, Radiat. Phys. Chem. **72**, 159 (2005).

[285] H. Iglev, A. Trifonov, A. Thaller, I. Buchvarov, T. Fiebig, and A. Laubereau, Chem. Phys. Lett. **403**, 198 (2005).

[286] X. Y. Chen and S. E. Bradforth, Annu. Rev. Phys. Chem. **59**, 203 (2008).

[287] Y.-I. Suzuki, H. Shen, Y. Tang, N. Kurahashi, K. Sekiguchi, T. Mizuno, and T. Suzuki, Chem. Sci. **2**, 1094 (2011).

[288] E. B. Krissinel and N. Agmon, J. Comput. Chem. **17**, 1085 (1996).

[289] R. N. Barnett, U. Landman, C. L. Cleveland, and J. Jortner, J. Chem. Phys. **88**, 4421 (1988).

[290] R. N. Barnett, U. Landman, C. L. Cleveland, and J. Jortner, J. Chem. Phys. **88**, 4429 (1988).

[291] J. R. R. Verlet, A. E. Bragg, A. Kammrath, O. Cheshnovsky, and D. M. Neumark, Science **307**, 93 (2005).

[292] J. R. R. Verlet, A. E. Bragg, A. Kammrath, O. Cheshnovsky, and D. M. Neumark, Science **310**, 1769 (2005).

[293] L. Ma, K. Majer, F. Chirot, and B. von Issendorff, J. Chem. Phys. **131**, 144303 (2009).

[294] R. M. Young, M. A. Yandell, S. B. King, and D. Neumark, J. Chem. Phys. **136**, 094304 (2012).

[295] H. Shen, N. Kurahashi, T. Horio, K. Sekiguchi, and T. Suzuki, Chem. Lett. **39**, 668 (2010).